

Structural deviation of hydrogenated graphene and multi-layer
graphene under high pressure



Mr. Teerachote Pakornchote

จุฬาลงกรณ์มหาวิทยาลัย
CHULALONGKORN UNIVERSITY

A Dissertation Submitted in Partial Fulfillment of the Requirements
for the Degree of Doctor of Philosophy in Physics
Department of Physics
Faculty of Science
Chulalongkorn University
Academic Year 2019
Copyright of Chulalongkorn University



จุฬาลงกรณ์มหาวิทยาลัย
CHULALONGKORN UNIVERSITY

การเขียนเบนเชิง โครงสร้างของไฮโดรจีเนตเตดกราฟีนและกราฟีนหลายชั้นภายใต้ความดันสูง



วิทยานิพนธ์นี้เป็นส่วนหนึ่งของการศึกษาตามหลักสูตรปริญญาวิทยาศาสตรดุษฎีบัณฑิต

สาขาวิชาฟิสิกส์ ภาควิชาฟิสิกส์

คณะวิทยาศาสตร์ จุฬาลงกรณ์มหาวิทยาลัย

ปีการศึกษา 2562

ลิขสิทธิ์ของจุฬาลงกรณ์มหาวิทยาลัย

Thesis Title	Structural deviation of hydrogenated graphene and multi-layer graphene under high pressure
By	Mr. Teerachote Pakornchote
Field of Study	Physics
Thesis Advisor	Associate Professor Dr. Thiti Bovornratanaraks
Thesis Co Advisor	Dr. Wutthikrai Busayaporn Dr. Alexander F. Goncharov

Accepted by the Faculty of Science, Chulalongkorn University in Partial Fulfillment of the Requirement for the Doctor of Philosophy

..... Dean of the Faculty of Science
(Professor Dr. POLKIT SANGVANICH)

DISSERTATION COMMITTEE

..... Chairman
(Associate Professor Dr. Parinya Karndumri)
..... Thesis Advisor
(Associate Professor Dr. Thiti Bovornratanaraks)
..... Thesis Co-Advisor
(Dr. Wutthikrai Busayaporn)
..... Thesis Co-Advisor
(Dr. Alexander F. Goncharov)
..... Examiner
(Associate Professor Dr. SAKUNTAM SANORPIM)
..... Examiner
(Dr. Thiti Taychatanapat)
..... External Examiner
(Assistant Professor Dr. Pongsakorn Kanjanaboos)

ธีรโชติ ภากรโชติ : การเบี่ยงเบนเชิงโครงสร้างของไฮโดรจีเนตเตดกราฟีนและกราฟีนหลายชั้นภายใต้ความดันสูง. (Structural deviation of hydrogenated graphene and multi-layer graphene under high pressure) อ.ที่ปรึกษาหลัก : รศ. ดร.ชิตี บวรรัตนรักษ์, อ.ที่ปรึกษาร่วม : ดร.วุฒิไกร บุญยาพร,ดร.อเล็กซานเดอร์ กอนซารอฟ

กราฟีนเป็นวัสดุที่เกิดจากอะตอมคาร์บอนเรียงตัวเป็นแผ่นแบบรังผึ้งและมีลักษณะเหมือนชั้นของกราไฟต์ กราฟีนมีสมบัติที่โดดเด่นหลายอย่างที่หากนำไปรวมกับวัสดุอื่นจะช่วยเพิ่มประสิทธิภาพการทำงานของวัสดุเชิงประกอบนั้นได้ อย่างไรก็ตามกราฟีนเป็นวัสดุกึ่งโลหะที่ทำให้การยุบตัวของมันถูกจำกัด เพื่อขยายขีดความสามารถของกราฟีน ไฮโดรเจนถูกนำผสมกับกราฟีนโดยอะตอมไฮโดรเจนและอะตอมคาร์บอนจะทำพันธะผสมแบบ sp^3 ซึ่งทำให้โครงสร้างของกราฟีนเปลี่ยนไป การเติมไฮโดรเจนทำให้เกิดช่องว่างพลังงานและแมกนิตาเซชันซึ่งเป็นการเปิดประตูสู่การประยุกต์ใช้อุปกรณ์สารกึ่งตัวนำและสปินโทรนิก คุณสมบัติของไฮโดรจีเนตเตดกราฟีนสามารถถูกปรับได้โดยการใช้พลาสมาหรือการอบด้วยความร้อนเพื่อเพิ่มหรือลดความหนาแน่นของไฮโดรเจนบนพื้นผิวกราฟีน ดังนั้นความหนาแน่นของไฮโดรเจนจึงมีบทบาทสำคัญในปรับเปลี่ยนคุณสมบัติและความเสถียรของไฮโดรจีเนตเตดกราฟีน ในวิทยานิพนธ์นี้เราได้ศึกษาความเสถียรภาพเชิงสถานะและเส้นทางการเปลี่ยนสถานะของไฮโดรจีเนตเตดกราฟีนแบบชั้นเดียวและไฮโดรจีเนตเตดกราฟีนแบบสองชั้นทั้งทางทฤษฎีและการทดลอง ส่วนแรกคือการศึกษาในเชิงทฤษฎี โดยเราได้ทำการศึกษาถึงพลังงานการก่อตัวของไฮโดรจีเนตเตดกราฟีนที่มีปริมาณของไฮโดรเจนต่างๆ กันด้วยทฤษฎีฟังก์ชันนัลของความหนาแน่น ผลที่ค้นพบคือไฮโดรจีเนตเตดกราฟีนไม่มีเสถียรภาพเชิงพลังงานแต่มีเสถียรภาพเชิงพลศาสตร์ ทั้งนี้เรายังได้วิเคราะห์การสั่นของโครงสร้างคริสตัลเพื่อใช้เป็นอัตลักษณ์ของสเปกตรัมรามานและอินฟราเรดเพื่อการค้นหาในการทดลองต่อไปในอนาคต ส่วนที่สองคือการศึกษาด้วยการทดลอง ไฮโดรจีเนตเตดกราฟีนที่มีความหนาแน่นของไฮโดรเจนสูงถูกสังเคราะห์โดยการยิงเลเซอร์เพื่อให้ความร้อนภายใต้ความดันสูง จากการทดลองพบว่าหากเราให้ความร้อนที่ความดันสูงขึ้นส่งผลให้ความหนาแน่นของไฮโดรเจนที่เกาะอยู่บนผิวกราฟีนเพิ่มขึ้นตาม นอกจากนี้เรายังพบว่าแผ่นกราฟีนหลุดออกจากวัสดุฐานรองหลังจากได้รับความร้อนซึ่งสามารถอธิบายได้ด้วยแบบจำลองที่ถูกนำเสนอในงานวิจัยชิ้นนี้



สาขาวิชา	ฟิสิกส์	ลายมือชื่อนิสิต
ปีการศึกษา	2562
		ลายมือชื่อ อ.ที่ปรึกษาหลัก
		ลายมือชื่อ อ.ที่ปรึกษาร่วม
		ลายมือชื่อ อ.ที่ปรึกษาร่วม

5972822623 : MAJOR PHYSICS

KEYWORD Hydrogenated graphene, High pressure, Phase transition, Raman
D: spectroscopy, Vibrational analysis

Teerachote Pakornchote : Structural deviation of hydrogenated graphene and multi-layer graphene under high pressure. Advisor: Assoc. Prof. Dr. Thiti Bovornratanaraks Co-advisor: Dr. Wutthikrai Busayaporn, Dr. Alexander F. Goncharov

Graphene, a layer of graphite, has marvelous properties that can enhance the performance of its composite materials. To broaden the capability of its applications, the adatoms are introduced onto graphene to create such distinguish property. Hydrogenated graphene is a hydrogen deposition on graphene forming sp^3 -hybridization between carbon and hydrogen atoms and deviating the structure of graphene. Partial hydrogenation induces the energy gap and the magnetization of graphene which opens the door to many applications, *e.g.* semiconducting and spintronic devices. The properties of hydrogenated graphene can be tuned by either plasma bombarding or thermal annealing to raise or reduce, respectively, the number of hydrogen atoms on a graphene surface. Therefore, the hydrogen concentration plays a central role in tunable properties and phase stability of hydrogenated graphene. In this thesis, we studied the phase stability and the phase transition pathway of hydrogenated single-layer graphene and hydrogenated bilayer graphene on theoretical and experimental bases. In the theoretical part, the formation energies of the hydrogenated graphenes with various hydrogen concentrations were obtained using density functional theory (DFT). The phase stabilities are portrayed by the convex hull which is based on the thermodynamic principle. Most of the phases in this study are not energetically favorable, while some of the phases can be stabilized by compressive strain. However, many of them are still dynamically stable. The vibrational analysis was performed to show the fingerprint of possible Raman and infrared (IR) spectrum for guiding the experiment. In the experimental part, the highly hydrogenated graphene was synthesized using laser-heating at high pressure. As a result, the hydrogenation could occur more when the sample was compressed at a higher pressure in the hydrogen environment presenting the hydrogenation pathway toward fully hydrogenated graphene. We also model the possible slippery of graphene from its substrate and show the possible hole-doping of hydrogenated graphene at high pressure.

Field of Study: Physics

Student's Signature

.....

Academic 2019

Advisor's Signature

Year:

.....

Co-advisor's Signature

.....

Co-advisor's Signature

.....

ACKNOWLEDGEMENTS

I would like to dedicate this dissertation to my parents and siblings who are always support me. I would like to thank Assoc.Prof.Dr. Thiti Bovoranaraks, Assoc.Prof.Dr. Udomsilp Pinsook and Dr. Wutthikrai Busayaporn who always give me good instructions whenever I need some advises, Dr. Alexander F. Goncharov and Dr. Zachary M. Geballe who always help me get through delicate and cumbersome high-pressure experiments, Dr. Annop Ektarawong who gave me a hand to perform a part of simulation and especially edited my language easier to be understood. I am also very grateful to labmates in Extreme Condition Research Laboratory for great discussion and good time eating. Last but not least, I really appreciate the time when I was at Carnegie Institution for Science that I met many good friends who hung out, traveled, etc. together with me.

Many thanks.

Teerachote Pakornchote

TABLE OF CONTENTS

	Page
ABSTRACT (THAI)	iii
ABSTRACT (ENGLISH)	iv
ACKNOWLEDGEMENTS	v
TABLE OF CONTENTS	vi
1 Introduction.....	1
1.1 Characterization	1
1.2 Strain and high-pressure experiments.....	2
1.3 Hydrogenation	3
1.4 Magnetism	3
1.5 Superhardness	4
1.6 Aim of this thesis	4
2 Theory for <i>ab-initio</i> calculation.....	6
2.1 Hamiltonian of condensed matter systems	6
2.2 Density functional theory.....	6
2.2.1 Hohenberg-Kohn theorem.....	7
2.2.2 Kohn-Sham scheme.....	8
2.3 Plane-wave basis set	9
2.4 Pseudopotential.....	9
2.5 Pulay stress	10
3 Dynamical and thermodynamic stabilities.....	11
3.1 Finite displacement method.....	11
3.2 Vibrational energy and entropy	12
3.3 Thermodynamics stability.....	13
4 Raman spectroscopy on graphene and defective graphene.....	15
4.1 Raman scattering.....	15

4.2 Defect concentration	18
4.3 Types of the defect in graphene	20
4.4 Vibrational analysis	21
5 Phase stabilities of hydrogenated BLG	23
5.1 Overview	23
5.1.1 Crystal structure and energy contours	23
5.1.2 Electronic band structure	26
5.2 Phase stabilities	29
5.2.1 Thermodynamic stability	29
5.2.2 Dynamical stability	30
5.3 Crystal vibration	31
5.3.1 Vibrational analysis	31
5.3.2 Designation of vibrational schemes	34
6 Phase stabilities of hydrogenated SLG	36
6.1 Overview	36
6.2 Thermodynamic stability	37
7 Slipping Model	40
8 Hydrogenation pathway of hydrogenated SLG at high pressure	45
8.1 Experimental procedures	45
8.2 Ruby pressure gauge	47
8.3 Temperature estimation	47
8.4 Residuals of hydrogenation	48
8.5 Pathway toward graphane at high pressure	51
8.6 Total stress and frictional stress on SLG	55
8.7 Correlation between ωG and $\omega 2D$	58
8.8 Massive hydrogenation or detachment from the substrate?	59
9 Conclusion	62
Appendix A: List of Abbreviations	63
REFERENCES	64

VITA.....72



จุฬาลงกรณ์มหาวิทยาลัย
CHULALONGKORN UNIVERSITY

1 Introduction

2-dimensional (2d) material is a type of material that has a few atoms thick. Their thinness could be beneficial for fabricating smaller electronic devices. The first 2d material discovered is graphene composing of one layer of C atoms forming a honeycomb structure [1]. Two low energy electronic band structure of graphene disperse linearly with wave vector, forming a Dirac cone in the reciprocal space. Two linear electronic bands of graphene cross each other at the K points, resulting in a zero energy gap. The low-energy electrons therefore behave as a massless Dirac particle [2]. However, the impurities and the surface roughness of the substrate supporting graphene increase the scattering rate of electrons and so reduce electron mobility tremendously [3, 4]. The ripples of the graphene sheet, produced by the flexural mode of acoustic phonons [5], also distort the graphene structure and generate the charge puddles which further decrease the electron mobility [6]. A layer of boron nitride was introduced to encapsulate the graphene sheet to reduce the surface roughness and the ripples in graphene [7, 8]. This method can improve the electron mobility and conductivity of graphene efficiently [8].

Applications of graphene expand into many fields of research especially in the improvement of electronic devices, *i.e.* transparent electrode, Schottky diode, *etc.* However, most semiconductor devices such as a normal diode require a material with a band gap. Therefore, making use of graphene in these devices is obscured by its semi-metallic property. Even though graphene has many other applications that do not involve electronic devices, *i.e.* graphene membrane, graphene ink, *etc.* Some of these applications do not require graphene to be single-layer, since they do not require such high quality found in single layer graphene. Therefore, the term ‘graphene’, herein, includes single-layer graphene (SLG), and multilayer graphene which are bilayer graphene (BLG) and few-layer graphene (3-5 layers). The specific terms such as SLG then will be used in the case that requires a specification of the number of layers.

In this thesis, we performed the theoretical simulation and the experiment to study hydrogenated graphene which can be applied to many applications. Background, motivation, and the backbone of the research in this thesis, are summarized below.

1.1 Characterization

Raman spectroscopy is a typical method to observe graphene. Two main Raman peaks of graphene are G peak at 1580 cm^{-1} and 2D peak at 2800 cm^{-1} [9], where 2D peak can be used to verify a number of graphene layers [9, 10]. For example, two stacked layers of graphene split a sharp single 2D peak of one-layer into a four convoluting peak of two-layer [10, 11]. More substitute peaks, D and D', appearing in the Raman spectrum of graphene, are enhanced by defects [9], so they can be used to verify the quality of graphene lattice [12].

The multiwavelength laser can be used to study the intrinsic property of graphene. The dispersions of G and D peaks, which are the variation of the peak position with the excitation energy of the laser, are 7 and 50 cm^{-1}/eV , respectively. Since the 2D peak is a double mode of D peak, the dispersion of the 2D peak is 100 cm^{-1}/eV [9].

Furthermore, the structure of graphene can be observed by a scanning electron microscope (SEM) and a transmission electron microscope (TEM). SEM can probe the real space pattern of the atomic arrangement of graphene which defects and residuals can be pointed out. TEM diffraction can obtain the Bragg's peak of graphene showing the reciprocal plane of graphene which is useful for determining intrinsic property, *i.e.* lattice parameter, twisted formation, and roughness [7, 13-15].

1.2 Strain and high-pressure experiments

The covalent bonds between in-plane carbon atoms are very strong, so the tensile strength of graphene is remarkably high. Graphene can be stretched up to ~ 21% tensile strain before failure [16]. If graphene is applied by biaxial tensile and compressive strain, respectively, G and 2D peaks will shift to lower and higher frequencies. However, if graphene is applied by uniaxial strain, the G peak will split into G^+ and G^- peaks [17, 18]. Under uniaxial strain, 2D peak also splits into $2D^+$ and $2D^-$ peaks, if the polarized laser is used. $2D^+$ and $2D^-$ peaks appear in the Raman spectrum alternately depending on a polarized angle; only $2D^+$ peak for 90° and 270° polarized angles, only $2D^-$ peak for 0° and 180° polarized angles, and $2D^+$ and $2D^-$ peaks simultaneously for other polarized angles [19]. The Grüneisen parameter can be obtained from the shifting rate of G and 2D peaks with respect to strain. The G and 2D peaks also shift depending on the number of layers of graphene, where the shifting rate of SLG is higher than graphite. If the number of layers of graphene increases, the shifting rates of G and 2D peaks then lower toward those of graphite [20].

The study on compressively strained graphene is more difficult than tensile strain, because the compressive strain may cause bulking or corrugation on graphene which leads to incorrect interpretation. A diamond anvil cell (DAC) is a device to generate high pressure in a cavity at a center of the device, where the homogeneity of the pressure depends on the pressure transmitting medium (PTM) that transfers pressure from the anvil onto the sample. In the tensile strain experiment, the strain can be determined directly from the piezo device by assuming that graphene is not slippery from its substrate [17]. In contrast, since graphene in DAC cannot be observed by SEM and TEM, its structure or strain cannot be determined directly. Raman spectroscopy is the tool to probe graphene in DAC if any changes happen.

Under high pressure, the rate of change of G peak depends on the substrate of SLG originated from a difference in the interaction between SLG and its

substrate [21]. The PTM may attribute to charge doping on graphene, however, the argument of this phenomena still proceeds [22, 23].

1.3 Hydrogenation

To engineer the bandgap of graphene, hydrogen plasma is used to introduced H atoms onto graphene in order to create hydrogenated graphene [24, 25] and opens its band gap confirmed by angle-resolved photoemission spectroscopy (ARPES) [26, 27]. The band gap of hydrogenated graphene can be tuned by varying an amount of hydrogen coverage [28-30]. Hydrogenated graphene can be reversed to graphene by annealing.

Even Raman spectroscopy is a convenient tool to probe graphene, an interpretation of Raman spectrum of hydrogenated graphene is ambiguous (see more discussion in section 4.3). The spectrum can lead to many interpretations such as vacancy-defect, edge-defect or sp^3 -bonding. Hydrogen residuals on graphene can be confirmed by many techniques such as x-ray photoemission (XPS), electron energy loss spectroscopy (EELS) [25, 29, 31]. The binding energy is used to distinguish types of C-H dangling [24, 27, 31].

Full coverage of H atoms on graphene has a stoichiometry C_2H_2 which is a fully hydrogenated graphene or a graphane. Theoretical study shows that it has such a wide band gap [32], however, it has not been synthesized successfully.

1.4 Magnetism

The perfect honeycomb graphene and graphite have no magnetic property, but their magnetism can be induced by creating defects and/or disorder in their crystal structures. The magnetism in graphene is also attributed by corrugations on the substrate surface creating bulging of the graphene sheet, increasing electron energy densities of Landau level and in result generating a pseudomagnetic field [33]. Moreover, the magnetization of graphene can occur by several reasons, *i.e.* sp^3 functionalization [34-38], vacancy-defect [39-41], and Stone-Wales defect [42].

The theoretical study shows that the half fully hydrogenated SLG obtains a speed of spin transport as high as bulk metal oxide, *i.e.* GaAs [43]. To engineer H atoms on SLG, a STM tip is used to pick H atom on to specific position on SLG to create magnetizations in SLG [36]. A number of magnetizations depend on a difference in a number of H atoms deposited on graphene between two sublattices.

1.5 Superhardness

Hardness is a physical property of materials to resist an indented force. Some carbon materials, *i.e.* diamond, and tetragonal amorphous carbon, have excessive hardness because of sp^3 -bonding between C atoms. Even SLG has high tensile strength [44] making it tough to be torn, it is not difficult to be indented deeply. On the contrary, for BLG, C atoms between layers can form sp^3 bonding when it is being indented [45-47]. The sp^3 carbon form of BLG hardens its substrate. However, if the indentation is pulled out, the sp^3 form cannot be maintained [45]. The process of AB- and AA-stacked BLG forming sp^3 -bonding is herein a diamondization, and its product is diamondene and lonsdaleitene, respectively, which are derived from diamond and lonsdaleite.

The theoretical study shows that diamondene cannot be stable under normal circumstances, whereas without the indentation, it will transform to BLG [48]. Functional groups, *i.e.* H atom, OH molecule, must be introduced onto the diamondene surface to maintain sp^3 bonding between C atoms. Partially functionalized diamondene is reported to be synthesized successfully at 5 GPa [49]. However, the recent study shows that the highly hydrogenated few-layer graphene can be synthesized using the H deposition technique as evidenced by the Raman peak at ~ 1100 , ~ 1300 cm^{-1} representing C-C sp^3 bonding and the infrared (IR) peak at ~ 2900 cm^{-1} representing C-H stretching mode [50].

1.6 Aim of this thesis

The promising properties of hydrogenated graphene have been shown by previous theoretical and experimental works. However, the highly hydrogenated graphene, which has distinguished property theoretically, has not been synthesized successfully. Therefore, this thesis aims to seek for a possibility to synthesize highly hydrogenated graphene theoretically and experimentally. In the theoretical part, the simulation has been performed to look for the condition, that improves the stability of hydrogenated graphene, guiding the experimental synthesis. In the experimental part, high pressure has been applied onto SLG growth on Cu substrate in hydrogen medium, and laser heating technique has been applied to DAC to stimulate chemical reaction between hydrogen and SLG inside the pressure cavity.

Since the thesis contains such bunch of information, the detail has been divided into 7 chapters; Chapter 2 is a brief explanation about density functional theory (DFT) which is a theoretical basis of results in Chapters 5 and 6, Chapter 3 presents, some theories in thermodynamics and condensed matter physics used to study the phase stability, Chapter 4 depicts the theory in Raman spectroscopy which is beneficial for understanding and analyzing the experimental results, Chapters 5 and 6 shows the results and discussions of the phase diagrams and the phase stabilities of hydrogenated BLG and SLG, respectively, in theoretical aspect, Chapter 7 presents a mathematical approach to explain stress between graphene and its substrate which is beneficial for

explaining the experimental work, and Chapter 8 shows the experimental work attempting to synthesize highly hydrogenated graphene using high pressure and temperature.



2 Theory for *ab-initio* calculation

Density functional theory (DFT) is a theory establishing the energy of the many electrons system in a functional form which has an electron density as an argument. The electron density can be evaluated using the self-consistence field (scf) method. The theory is very powerful because it decouples the parameters to be solved into a function form of the electron density which is computationally efficient. The trade-off is that an exact functional form of the coupling term, an exchange-correlation, has not yet been solved, so many approximated forms that give decent results are used instead. This theory is very powerful because the energy and the electron density taken from scf method can be used to further determine many properties of the condensed matter system which is advantageous for guiding experiments.

2.1 Hamiltonian of condensed matter systems

In quantum mechanics, the energy of the condensed matter system can be solved using time-independent Schrödinger's equation (TISE) with known Hamiltonian. However, the eigenvalues and the eigenvectors with many variables, which are the coordinates of nuclei and electrons, can be evaluated cumbersome. Since the interaction between atoms is mainly from the valence electrons, Born-Oppenheimer approximation, used to separate the electronic and nuclei part, is acquired to reduce the number of variables. Thus, only the electronic part of the Hamiltonian of condensed matter systems will be considered as

$$H = -\frac{1}{2} \sum_{i=1}^N \nabla_i^2 + \sum_{i=1}^N v(\mathbf{r}_i) + \sum_{i<j}^N \frac{1}{r_{ij}} \quad (2.1)$$

where the first term is the kinetic energy of the electrons in the system, the second term is the external potential due to nuclei acting on an electron i , and the third term is the Coulomb potential between electrons i and j . Therefore, the electronic wavefunction can be solved using TISE as

$$H\Psi(\mathbf{r}_1, \mathbf{r}_2, \dots, \mathbf{r}_N) = E\Psi(\mathbf{r}_1, \mathbf{r}_2, \dots, \mathbf{r}_N), \quad (2.2)$$

By solving the above equation, we will obtain the eigenenergy E and the wavefunction of the electrons in the system Ψ where \mathbf{r}_i is a position of an electron i . Even though only the electronic part is considered, some systems, *i.e.* B, C, Au, Ag, *etc.*, still contain too many electrons to be evaluated efficiently by a computer.

2.2 Density functional theory

One N-body problem in the previous section consumes computational time tremendously. To subside computational time, it must be transformed into N problems

of one-body by exploiting the Hohenberg-Kohn theorem [51] and Kohn-Sham (KS) scheme [52]. These two ideas are the backbone of the density functional theory (DFT) helping us to solve the electron density and the ground state energy of the system efficiently using the scf method.

2.2.1 Hohenberg-Kohn theorem

1) Uniqueness theorem

The external potential, $v(\mathbf{r})$, is uniqueness with the electron density. Thus, any atomic, molecular and condensed matter systems have their particular electron density by mean of no two systems share the same electron density. A short proof starts by setting the electron density of two systems, which have the same number of electrons, are alike,

$$\rho(\mathbf{r}) = \langle \Psi | \Psi \rangle = \langle \Psi' | \Psi' \rangle \quad (2.3)$$

where $|\Psi\rangle$ and $|\Psi'\rangle$ are wavefunctions of two different systems and $\rho(\mathbf{r})$ is the electron density. The Hamiltonians of two systems in Equation (2.1) are set to be different by the external potential, $v(\mathbf{r}_i)$ and $v'(\mathbf{r}_i)$, so

$$E_0 = \langle \Psi | H | \Psi \rangle = F[n] + \int \rho(\mathbf{r})v(\mathbf{r}) d\mathbf{r} \quad (2.4)$$

$$E'_0 = \langle \Psi' | H' | \Psi' \rangle = F[n] + \int \rho(\mathbf{r})v'(\mathbf{r}) d\mathbf{r} \quad (2.5)$$

where E_0 and E'_0 are the ground state energy of two different systems corresponding to their eigenfunction, $|\Psi\rangle$ and $|\Psi'\rangle$, respectively, and

$$\begin{aligned} F[n] &= \left\langle \Psi \left| -\frac{1}{2} \sum_{i=1}^N \nabla_i^2 + \sum_{i<j}^N \frac{1}{r_{ij}} \right| \Psi \right\rangle \\ &= \left\langle \Psi' \left| -\frac{1}{2} \sum_{i=1}^N \nabla_i^2 + \sum_{i<j}^N \frac{1}{r_{ij}} \right| \Psi' \right\rangle \end{aligned} \quad (2.6)$$

$$\int \rho(\mathbf{r})v(\mathbf{r}) d\mathbf{r} = \sum_{i=1}^N \langle \Psi | v(\mathbf{r}_i) | \Psi \rangle = \int \Psi^*(\mathbf{r}_i)\Psi(\mathbf{r}_i)v(\mathbf{r}_i) d\mathbf{r}_1 \cdots d\mathbf{r}_N \quad (2.7)$$

$$\begin{aligned} \int \rho(\mathbf{r})v'(\mathbf{r}) d\mathbf{r} &= \sum_{i=1}^N \langle \Psi | v'(\mathbf{r}_i) | \Psi \rangle \\ &= \int \Psi^*(\mathbf{r}_i)\Psi(\mathbf{r}_i)v'(\mathbf{r}_i) d\mathbf{r}_1 \cdots d\mathbf{r}_N \end{aligned} \quad (2.8)$$

where $\mathbf{r} \equiv \mathbf{r}_1$. Therefore

$$E_0 < \langle \Psi' | H | \Psi' \rangle = E'_0 + \int \rho(\mathbf{r})[v(\mathbf{r}) - v'(\mathbf{r})] d\mathbf{r} \quad (2.9)$$

$$E'_0 < \langle \Psi | H' | \Psi \rangle = E_0 - \int \rho(\mathbf{r}) [v(\mathbf{r}) - v'(\mathbf{r})] d\mathbf{r} \quad (2.10)$$

By combining Equations (2.9) and (2.10), one would see the contradiction leading to the impossibility that two systems, which have different external potentials, have the same electron density.

2) Ground state energy theorem

By the variational principle, a trial electron density, which is not a true electron density of the system, will yield the energy higher than the ground state energy of the system. The true electron density of the system will yield the ground state energy which is the lowest energy that the energy functional could be evaluated.

$$E_0 = E[\rho_{true}(\mathbf{r})] \leq E[\rho_{trial}(\mathbf{r})] \quad (2.11)$$

where $E[\rho(\mathbf{r})]$ is the energy functional.

2.2.2 Kohn-Sham scheme

Because solving the interacting electrons is still unwieldy, so Kohn and Sham [52] suggested using non-interacting particles instead. By exploiting the Hohenberg-Kohn theorem, we can choose the non-interacting particle system which shares similar external potential with the interacting electron system. Thus, the density of non-interacting particles would be the same as the electron density of the interacting electron system. The density formed from the non-interacting particles in the system can be written as

$$\rho(\mathbf{r}) = \sum_i^N \langle \Psi_i^{KS} | \Psi_i^{KS} \rangle \quad (2.12)$$

where $|\Psi_i^{KS}\rangle$ is a wavefunction of the non-interacting particle or Kohn-Sham (KS) wavefunction.

Non-interacting particles are considered to move in the effective field

$$v_{eff}(\mathbf{r}) = v_{ext}(\mathbf{r}) + \int \frac{\rho(\mathbf{r}')}{|\mathbf{r} - \mathbf{r}'|} d\mathbf{r}' + v_{xc}(\mathbf{r}) \quad (2.13)$$

where $v_{ext}(\mathbf{r})$ and $v_{xc}(\mathbf{r})$ are the external potential which is an effect from the nuclei and the exchange-correlation potential, respectively, and the second term on the right-hand side is a classical part of Coulomb's potential. The crucial role of v_{xc} is to fulfill the lost interaction from the non-interacting particle system. The first two terms on the right-hand side of Equation (2.13) are known formulas. However, the exact formula of v_{xc} has not yet settle, so it is explained by approximations, for example, local density approximation (LDA), and generalized gradient approximation (GGA).

Explicitly, the TISE of non-interacting particle system or KS equation will be

$$\left[-\frac{1}{2}\nabla^2 + v_{eff}(\mathbf{r})\right]|\Psi_i^{KS}\rangle = \varepsilon_i|\Psi_i^{KS}\rangle \quad (2.14)$$

where the first term on the left-hand side is a kinetic energy operator, and ε_i is an energy of one non-interacting particle. It is worth to note that Equation (2.12) is no longer the Schrödinger equation because its eigenfunction is not of an electron but non-interacting particle. By iteratively solving Equations (2.12), (2.13) and (2.14) known as scf method, we will obtain the density which is equivalence to the electron density of the real system by a succession of Hohenberg-Kohn theorem. The total energy of the system can be determined by

$$E = \sum_i^N \varepsilon_i = - \sum_i^N \langle \Psi_i^{KS} | \frac{1}{2} \nabla^2 | \Psi_i^{KS} \rangle + \int v_{eff}(\mathbf{r})\rho(\mathbf{r})d\mathbf{r} \quad (2.15)$$

when $\rho(\mathbf{r})$, obtained from the scf method, yields the lowest energy calculated using Equation (2.15), while it is implied to be the true electron density of the system.

2.3 Plane-wave basis set

In order to solve the KS equation, the trial wavefunction must be preliminary, and its function form must be known. The atoms in the crystal structure arrange periodically expanding in an infinite space, so the potential energy is also periodic. The wavefunction form that satisfies the periodic potential is in a special form like a plane-wave,

$$\psi_{\mathbf{k}}(\mathbf{r}) = u_{\mathbf{k}}(\mathbf{r}) \exp(i\mathbf{k} \cdot \mathbf{r}) \quad (2.16)$$

Hereby, the plane-wave basis set is used for KS wavefunction as

$$\Psi(\mathbf{r}) = \sum_{jk} C_{jk}(\mathbf{r}) \exp(i(\mathbf{k} + \mathbf{G}_j) \cdot \mathbf{r}) \quad (2.17)$$

where \mathbf{G}_j is a translational vector in reciprocal space and $C_{jk}(\mathbf{r})$ is a coefficient of the plane wave which must be assigned for the trial wavefunction. By virtue of quantum mechanics, the wavefunction can be projected into any form of basis set as long as it satisfies Hilbert's space conditions [53].

2.4 Pseudopotential

The wavefunction of the electron in the atom is very smooth far from the core and very wavy nearby the core. Since we choose the plane-wave as a basis set, a large basis set must be used to correct the wavy feature to imitate the true electron wavefunction of the atom. The wavefunction of the core electron does not change in bonding, but the wavefunction of the valence electron does. To reduce the computational cost, the wavefunction of the core electron is separated from the valence electron and frozen in

the calculation. Therefore, the wavefunction of the valence electron will be solved solely. The wavefunction, that its core wavefunction is subtracted, is called pseudo wavefunction,

$$|\Psi_{ps}\rangle = |\Psi\rangle - \sum |\Psi_c\rangle \langle \Psi_c | \Psi_{ps}\rangle \quad (2.18)$$

where $|\Psi\rangle$ is the wavefunction of all electrons, and $|\Psi_c\rangle$ is the wavefunction of core electrons. And we can treat only valence electron wavefunction by the condition that

$$|\Psi_{ps}\rangle = |\Psi\rangle \text{ for } r \geq r_c \quad (2.19)$$

where r_c is a cut-off radius of the core electron.

In the projector augmented wave (PAW) method [54, 55], the pseudo wavefunction can be transformed to all electrons wavefunction by

$$|\Psi\rangle = \hat{\mathcal{J}} |\Psi_{ps}\rangle \quad (2.20)$$

and

$$\hat{\mathcal{J}} = 1 + \sum_R \hat{\mathcal{J}}_R \quad (2.21)$$

where $\hat{\mathcal{J}}_R$ is a projector in an augmented region Ω_R which is a region with the radius r_c , otherwise, it is zero.

2.5 Pulay stress

To find the optimal structure at a particular pressure, the internal pressure of the system needs to be balanced with the external pressure. Pulay stress can be considered as internal stress calculated using Hellmann-Feynman theorem

$$F_{ij} = -\frac{dE}{dr_{ij}} = -\frac{d}{dr_{ij}} \langle \Psi_i^{KS} | \hat{H} | \Psi_i^{KS} \rangle \quad (2.22)$$

where F_{ij} is a force acting on each atom in a unit cell in direction $j = 1, 2, 3$. Pulay stress can be obtained by multiplication between the summation of forces on every atom in each direction and the area that is perpendicular to that force.

3 Dynamical and thermodynamic stabilities

3.1 Finite displacement method

The motion of the nucleus has been neglect in the DFT calculation. However, the nucleus has its movement vibrating around the equilibrium position. Because the nucleus vibrates with such small amplitude, so the Hamiltonian of the nucleus can be expanded around the equilibrium position using Taylor's series expansion as

$$H = \sum_{n\alpha i} \frac{M_\alpha}{2} \dot{s}_{n\alpha i}^2 + \frac{1}{2} \sum_{\substack{n\alpha i \\ n'\alpha' i'}} \Phi_{n\alpha i}^{n'\alpha' i'} s_{n\alpha i} s_{n'\alpha' i'} \quad (3.1)$$

where M_α is a mass of a α atom in a unit cell, $s_{n\alpha i}$ is a displacement of the α^{th} atom in n^{th} unit cell, and

$$\Phi_{n\alpha i}^{n'\alpha' i'} = \frac{\partial^2 V}{\partial R_{n\alpha i} \partial R_{n'\alpha' i'}} = - \frac{\partial F_{n'\alpha' i'}}{\partial R_{n\alpha i}} \quad (3.2)$$

where V is the potential energy, $R_{n\alpha i}$ is the atomic position in $i = x, y, z$ direction, and $F_{n\alpha i} = -\partial V / \partial R_{n\alpha i}$ is the force acting on that atom. The harmonic approximation is used to obtain the displacement as

$$s_{n\alpha i}(t) = \frac{1}{\sqrt{M_\alpha}} u_{n\alpha i} e^{-i\omega t} \quad (3.3)$$

where $u_{n\alpha i}$ is the amplitude of the vibration with angular frequency ω , and M_α is a mass of α^{th} atom. The equation of motion of the atom in the unit cell will be

$$\sum_{n'\alpha' i'} D_{n\alpha i}^{n'\alpha' i'} u_{n'\alpha' i'} = \omega^2 u_{n\alpha i} \quad (3.4)$$

where the operator on the left-hand side is a dynamical matrix,

$$D_{n\alpha i}^{n'\alpha' i'} = \frac{\Phi_{n\alpha i}^{n'\alpha' i'}}{\sqrt{M_\alpha M_{\alpha'}}} \quad (3.5)$$

If the dynamical matrix is determined, the eigenvalues, ω , which are phonon normal modes and phonon eigenvectors, $u_{n\alpha i}$, can be solved using Equation (3.4). The dynamical matrix in Equation (3.5) can be obtained using the finite displacement method as

$$\Phi_{n\alpha i}^{n'\alpha' i'} \cong - \frac{F_{n'\alpha' i'}(r_{n\alpha i} = \Delta R_{n\alpha i}) - F_{n'\alpha' i'}(r_{n\alpha i} = 0)}{\Delta R_{n\alpha i}} \quad (3.6)$$

The force of the atom in the unit cell which is displaced by $\Delta R_{n\alpha i}$, can be obtained using the Hellmann-Feynman theorem (see section 2.5).

3.2 Vibrational energy and entropy

The phonon or vibrational energy of each mode as a function temperature T can be calculated by

$$E_{iq}(T) = \hbar\omega_{iq} \left[\frac{1}{2} + n(\omega_{iq}, T) \right] \quad (3.7)$$

where ω_i is a phonon i mode at wave vector \mathbf{q} in the reciprocal space, and the phonon occupation number

$$n(\omega_{iq}, T) = \frac{1}{\exp(\hbar\omega_{iq}/k_B T) - 1} \quad (3.8)$$

Since the vibrational frequencies are continuous in the reciprocal space, the vibrational energy can be evaluated by the integration over the first Brillouin zone (in the reciprocal space) and all phonon modes as

$$E_{vib}(T) = \int_0^\infty \hbar\omega D(\omega) \left[\frac{1}{2} + n(\omega, T) \right] d\omega \quad (3.9)$$

where $D(\omega)$ is the phonon density of states. In the case of $T \rightarrow 0$, the phonon occupation number will be null, and Equation (3.9) becomes the zero-point energy

$$E_{zp} = \frac{\hbar}{2} \int_0^\infty \omega D(\omega) d\omega \quad (3.10)$$

Therefore, the total energy including the vibrational energy is

$$E(T) = E_{int} + E_{zp} + \int_0^\infty \frac{\hbar\omega}{\exp(\hbar\omega/k_B T) - 1} D(\omega) d\omega \quad (3.11)$$

where E_{int} is the internal energy of the system. And for 0 K, Equation (3.11) is reduced to

$$E(0) = E_{int} + E_{zp} \quad (3.12)$$

The occupation of each phonon can be considered as a microstate, so the vibrational partition function is

$$Z_{vib}(T) = \exp\left(-\frac{E_{zp}}{k_B T}\right) \prod_{iq} \frac{1}{1 - \exp(-\hbar\omega_{iq}/k_B T)} \quad (3.13)$$

The vibrational entropy can be obtained from the partition function by

$$S_{vib}(T) = \frac{\partial}{\partial T} [k_B T \ln(Z_{vib})] \quad (3.14)$$

Inserting Equation (3.13) into Equation (3.14), then

$$S_{vib}(T) = \int_0^{\infty} \frac{\hbar\omega/T}{\exp(\hbar\omega/k_B T) - 1} D(\omega) d\omega - k_B \int_0^{\infty} D(\omega) \ln \left[1 - \exp\left(-\frac{\hbar\omega}{k_B T}\right) \right] d\omega \quad (3.15)$$

The entropy is used to calculate the thermodynamic potential to look for phase stability which will be discussed in the next section.

3.3 Thermodynamics stability

In thermodynamics, the system, isolated from external influences such as heat bath and pressurization, will make itself to have the lowest internal energy and/or highest entropy. If the system connects to temperature and pressure reservoirs, the free energy or thermodynamics potential must be considered by transforming the energy as

$$E(S) \rightarrow G(T, P) \quad (3.16)$$

where $G(T, P)$ is the Gibbs free energy which can be expressed using Legendre's transformation as

$$G(T, P) = E(T) - TS(T) + PV \quad (3.17)$$

where V is the volume, T and P are the temperature and pressure reservoirs, respectively, connecting with the system, and the entropy

$$S(T) = S_{vib}(T) + S_{el}(T) + S_{mag}(T) + S_{conf}(T) + \dots \quad (3.18)$$

where terms on the right-hand side are the entropy of vibrations, electronic excitation, magnetic and configurations, respectively. Because most of the systems studied in this thesis are semiconductors, and magnetism is not included in the calculation, so $S_{el}(T)$ and $S_{mag}(T)$ can be neglected. $S_{conf}(T)$ comes up, if the system has a configuration of atomic arrangement more than one configuration. Herein, $S(T) \approx S_{vib}(T)$. Although, only energy attributed by vibrations is included in total energy as in Equation (3.11). Therefore, combining Equations (3.11), (3.15) and (3.17) then

$$G(T, P) = E_{int} + E_{zp} + k_B T \int_0^{\infty} D(\omega) \ln \left[1 - \exp\left(-\frac{\hbar\omega}{k_B T}\right) \right] d\omega + PV \quad (3.19)$$

The phase transition must satisfy the condition that

$$\Delta G(T, P) \leq 0 \quad (3.20)$$

By the above condition, the system will transform into the phase that has the lowest Gibbs free energy among all possible phases. In the reaction process, Gibbs free energy of formation is

$$\Delta G_{form}(A_m B_n) = \frac{G(A_m B_n) - mG(A \text{ system}) - nG(B \text{ system})}{m + n} \quad (3.21)$$

where A and B are the reactance, and $A_m B_n$ is the product with m proportion of A and n proportion of B . The product will be the phase that has the lowest ΔG_{form} .



4 Raman spectroscopy on graphene and defective graphene

4.1 Raman scattering

Raman spectroscopy is used to probe the alteration of the structure and/or chemical composition of the subject. Regularly, the laser with a wavelength in a range of UV-to-IR (ultraviolet to infrared) is used in Raman spectroscopy. In the experiment, the backscattering technique is used to detect the Raman signal where the incident and reflected lasers are in opposite directions. The photon scattering with the phonon obeys the energy and momentum conservations, then it returns to the detector with the energy lowered or risen by the phonon energy.

In quantum perspective, the photon comes to excite the electron creating an electron-hole ($e-h$) pair where the Stokes scattering is when the pair loses some of its energy to the phonon, the anti-Stokes scattering is when the pair gains some of its energy from the phonon, and the Rayleigh scattering is when the pair does not lose or gain the energy from the phonon. In the Raman experiment, the Stokes scattering is typically observed because the anti-Stokes scattering has a lower probability yielding lower intensity of Raman peak. Therefore, the Stokes scattering will be mainly discussed where the anti-Stokes is different by plus and minus signs in the conservation laws. In the laboratory frame, the phonon is considered as a rest mass, and the conservation of momentum is written by neglecting the intermediate process as

$$\mathbf{p}_{\text{photon},i} - \mathbf{p}_{\text{photon},s} = \mathbf{p}_{\text{phonon}} \quad (4.1)$$

where $\mathbf{p}_{\text{photon},i}$ and $\mathbf{p}_{\text{photon},s}$ are the momentums of the incident and scattering photons, respectively, and $\mathbf{p}_{\text{phonon}} = \hbar\mathbf{q}$, where \mathbf{q} is the phonon wave vector. And the conservation of energy is,

$$\hbar\omega_{\text{photon},i} - \hbar\omega_{\text{photon},s} = \hbar\omega_{\text{phonon}} \quad (4.2)$$

where $\omega_{\text{photon},i}$ and $\omega_{\text{photon},s}$ are the angular frequencies of the incident and scattering photons, respectively, and ω_{phonon} is the angular frequency of the scattering phonon. For the anti-Stokes scattering, the minus sign in front of the phonon term in Equations (4.1) and (4.2) will be changed to a plus sign (see scattering schemes in Figure 4-1).

The optical phonon frequencies of molecules/materials are typically in the terahertz (THz) scale. For example, the optical phonon of graphene at Γ -point is 47.37 THz or 0.1959 eV (for G peak) which in the case of Stokes scattering yields,

$$\hbar\omega_{\text{photon},s} - \hbar\omega_{\text{photon},i} = \hbar\omega_{\text{phonon}} = 0.1959 \text{ eV} \quad (4.3)$$

For the backscattering process, using Equations (4.1) and (4.3), the phonon wave vector that scatters with the photon can be obtained by,

$$|\mathbf{q}| = \frac{\Delta E_{\text{photon}}}{\hbar c} = \frac{1}{c} (\omega_{\text{photon},s} - \omega_{\text{photon},i}) = 1580 \text{ cm}^{-1}, \quad (4.4)$$

The order of magnitude of the momentum difference between incident and scattering photons is $\sim 10^3 \text{ cm}^{-1}$. In contrast, the zone boundary, such as K-point in a hexagonal lattice, is

$$|\mathbf{K}| = \pi/a = 1.30 \times 10^{12} \text{ cm}^{-1}, \quad (4.5)$$

where a is the lattice parameter of graphene which is 2.42 \AA . As a result, $|\mathbf{K}|$ is comparatively nine orders of magnitude higher than $|\mathbf{q}|$. To satisfy the conservation of momentum in Equation (4.1), only phonons around Γ -point, where $|\mathbf{\Gamma}| = 0 \text{ cm}^{-1}$ $|\mathbf{q}|$, are allowed to exchange the momentum and energy with the incident photon.

As aforementioned, a large magnitude of momentum is required to activate the phonon at K-point. Although several peaks such as D, D+D', 2D peaks, (mostly) contributed by phonons on Γ -M branch, can appear in the Raman spectrum of graphene by satisfying the two-phonon process [56],

$$\hbar\omega_{\text{photon},i} - \hbar\omega_{\text{photon},s} = \hbar\omega_{\text{phonon}} + \hbar\omega'_{\text{phonon}} \quad (4.6)$$

and

$$\mathbf{p}_{\text{photon},i} - \mathbf{p}_{\text{photon},s} = \mathbf{p}_{\text{phonon}} + \mathbf{p}'_{\text{phonon}} \quad (4.7)$$

Then, in the two-phonon process, the photon loses or gains the energies of two phonons. Although, the magnitude of the right-hand side in Equation (4.7) is still in the same order of magnitude as in Equation (4.1), so

$$(|\mathbf{q} + \mathbf{q}'| \approx 10^3) \ll (|\mathbf{K}| \approx 10^{12}) \quad (4.8)$$

Equation (4.7) allows that the phonon wave vector, \mathbf{q} , can have the magnitude as much as that of the zone boundary and cancels out with another phonon wave vector, \mathbf{q}' , which has the magnitude similar to $|\mathbf{q}|$, but with the opposite direction (see Figure 4-2). Two phonons hence can be any modes across the phonon dispersion as long as they satisfy Equations (4.6) and (4.7), so the energies of two phonons are not restricted to have the same energy. The summation of two phonon energies can result in broad range yielding broad Raman peak which typically merges with the background of the spectrum.

For 2D (2D') peaks, it comes up from the same two phonon scatterings of D (D') mode which its appearance will be discussed later. Thus, Equation (4.6) will be

$$\hbar\omega_{\text{photon},i} - \hbar\omega_{\text{photon},s} = 2\hbar\omega_{\text{phonon}} \quad (4.9)$$

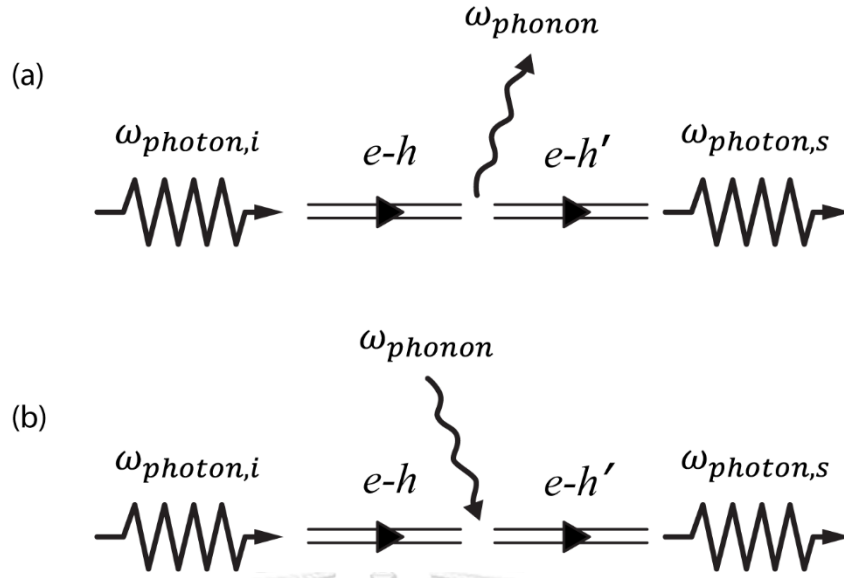


Figure 4-1 Quantum perspective of Raman scattering that the photon comes to excite the electron creating electron-hole ($e-h$) pair. (a) If the pair loses some of its energy to a phonon, the process is Stokes scattering. (b) If the pair gains some of its energy from phonon, the process is Anti-Stokes scattering. Typically, Raman experiment measures photons from the Stokes scattering which the population of the scattering photon is higher than Anti-Stokes scattering at room temperature.

and companions with the conservation of momentum in Equation (4.7) where $\mathbf{p}'_{\text{phonon}} = -\mathbf{p}_{\text{phonon}}$.

Even the two-phonon process can yield the photon scattering with any two phonons with arbitrary phonon wave vectors, some pairs are forbidden by Raman's selection rule (see the discussion in the next section) or give the very broad peak alike the background signal. One arbitrary pair of phonons appearing in the Raman spectrum of graphene is D+D'' peak contributed by two phonon modes which are D and D'' modes on Γ -K branch.

On the contrary, D and D' peaks legitimate the conservation laws by the aid of defects in graphene. Because the virtual phonon ('virtual' is herein used since the defect has no actual vibration) of the defect contains such zero energy, so the conservation of energy of the two-phonon process likes in one phonon-process as

$$\hbar\omega_{\text{photon},i} - \hbar\omega_{\text{photon},s} = \hbar\omega_{\text{phonon}} \quad (4.10)$$

but the conservation of momentum likes in the two-phonon process as

$$\mathbf{p}_{\text{photon},i} - \mathbf{p}_{\text{photon},s} = \mathbf{p}_{\text{phonon}} + \hbar\mathbf{q}_{\text{defect}} \quad (4.11)$$

where $\mathbf{q}_{\text{defect}}$ is the phonon wave vector of the virtual phonon of the defect. Therefore, the photon scattering with the phonon at K-point is conserved by the aid of the phonon wave vector of the virtual phonon of the defect in the opposite direction.

Previously, we discuss the photon scattering with the phonon by neglecting the internal process. As depicted in Figure 4-1, the incident phonon actually comes to excite the electron from the ground state. For the Stokes scattering process, the electron will lose some of its energy to the phonon and change the momentum by traveling through the reciprocal space if that phonon acquires (see Figure 4-2) during the recombination. SLG has two sublattices in the unit cell representing two high symmetry points, K and K', in the reciprocal space which are two neighboring points. To create D mode, the electron is restricted to travel across the intervalley (from K to K' and/or K' to K), while to create D' mode, the electron can travel across either the intravalley (from K to K and/or K' to K') or the intervalley (see Figure 4-2).

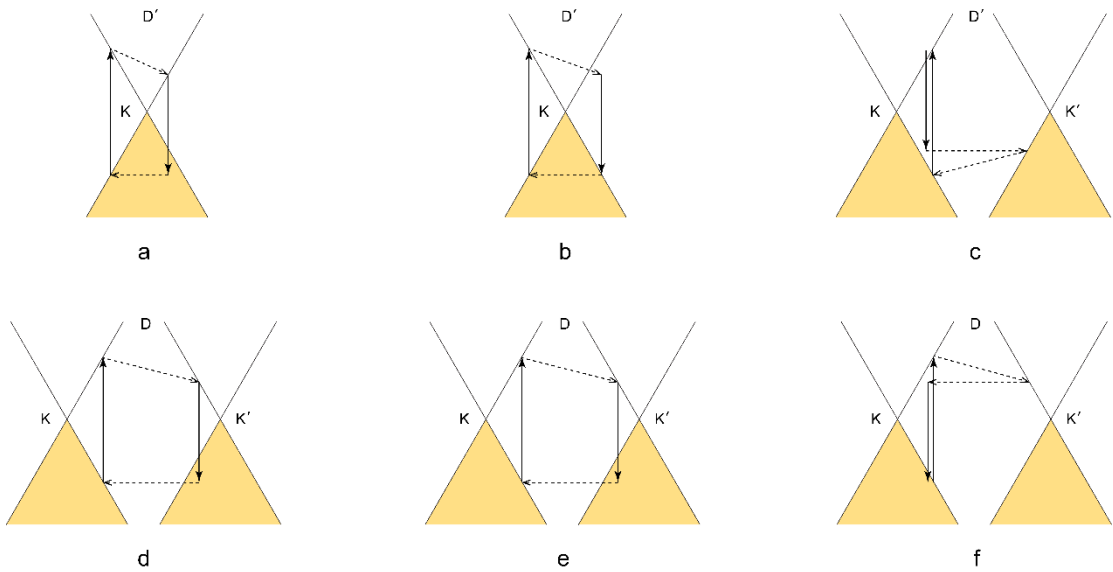


Figure 4-2 Some of the electron excitation and recombination diagrams in cases of scattering with (a)-(c) phonon D' mode and (d)-(f) phonon D mode.

Another Raman peak, enhanced by defects, is D+D', but this peak is appeared by a three-phonon process. The conservation laws of the three-phonon process are similar to those of the two-phonon process, but with additional energy and momentum. The three phonons of D+D' mode are D mode, D' mode, and the virtual phonon of the defect which is discussed elsewhere [9].

4.2 Defect concentration

The intensities of D and D' peaks can be used to determine the amount of defect by [57]

$$\frac{I(D)}{I(G)} = C_{A,D} \frac{r_A^2 - r_S^2}{r_A^2 - 2r_S^2} \left(e^{-\frac{\pi r_S^2}{L_D^2}} - e^{-\frac{\pi(r_A^2 - r_S^2)}{L_D^2}} \right) + C_{S,D} \left(1 - e^{-\frac{\pi r_S^2}{L_D^2}} \right) \quad (4.12)$$

$$\frac{I(D')}{I(G)} = C_{A,D'} \frac{r_A^2 - r_S^2}{r_A^2 - 2r_S^2} \left(e^{-\frac{\pi r_S^2}{L_D^2}} - e^{-\frac{\pi(r_A^2 - r_S^2)}{L_D^2}} \right) + C_{S,D'} \left(1 - e^{-\frac{\pi r_S^2}{L_D^2}} \right) \quad (4.13)$$

where $I(x)/I(G)$ is the intensity ratio between x and G peaks, $C_{A,x}$ relates to the ratio of electron-phonon coupling between x and G peaks and depends on the excitation energy (E_L) as $C_{A,x} \propto E_L^{-4}$ [12], $C_{S,x}$ is a parameter for x peak affecting significantly in the highly disordered limit (nevertheless, the interpretations of $C_{A,x}$ and $C_{S,x}$ are not well understanding), when $x = D$ or D' , L_D is an average distance between defects, converted to a defect concentration (N_D) by $N_D = 10^{14}/(\pi L_D^2)$, r_S is a radius of the structurally disordered region around the defect, and r_A is a radius larger than r_S when a subtraction between them is the mean free path of phonon D mode. Figure 4-3 illustrates the S-region, which is an area of structural disorder, and the A-region, which is an area of phonon D mode traveling during being activated [57]. Noting that if N_D is low, the D' peak will have low intensity and be barely resolved. Therefore, D peak is typically used to determine N_D .

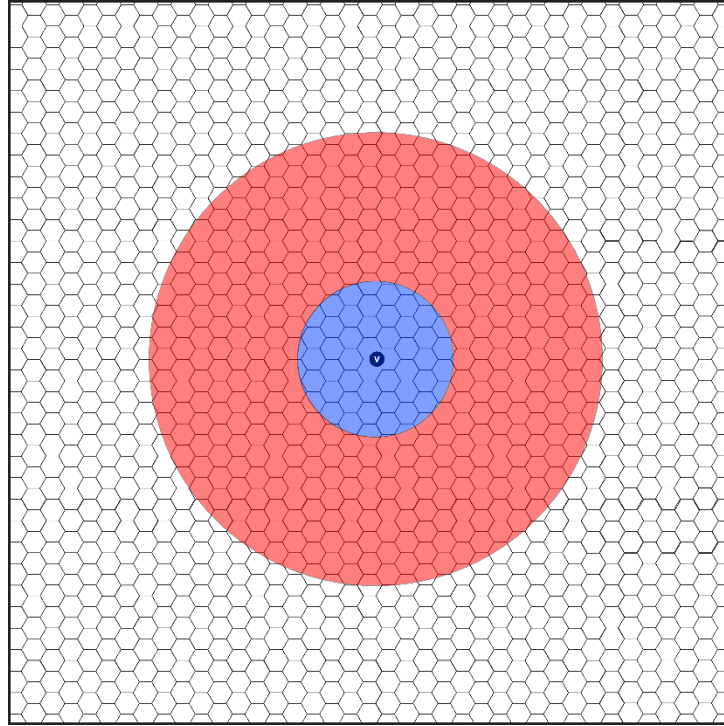


Figure 4-3 V at the center is either the sp^3 -defect or the void-defect. Blue circle is the S-region, and the red ring is the A-region.

4.3 Types of the defect in graphene

Three types of defect in graphene, will be discussed in this thesis, are sp^3 -, void-, and edge-defects. Their Raman spectra are similar since those three types of defects cause D and D' peaks appearing in the Raman spectrum. Even though the edge-defect limits the number of defects by the size of edges occurring on graphene flakes, the sp^3 - and void-defects can appear in a large amount. N_D occurring from sp^3 - and void-defects can be determined by $I(D)/I(G)$ using Equation (4.12). $I(D)/I(G)$ increases together with N_D if N_D is lower than $7 \times 10^{12} \text{ cm}^{-2}$, but $I(D)/I(G)$ decreases as N_D increasing if N_D is higher than $7 \times 10^{12} \text{ cm}^{-2}$ [56]. The former and latter phenomena are Stage 1 and Stage 2 of defective graphene, respectively. The number, $7 \times 10^{12} \text{ cm}^{-2}$, is not certain for multilayer graphene, since the threshold of N_D that separates two defective stages of defective/disordered graphite is different [58].

The sp^3 - and void-defects yield similar Raman spectra because both types of defects cause the alterations of C-C bond lengths in their vicinity which breaks the translational symmetry [9]. The C atoms and the impurity, *i.e.* H atom, O atom, F atom, *etc.*, forming sp^3 bonding, assemble as a massive collective particle causing the elastic scattering with the electron. The two-phonon process of sp^3 -defective graphene, caused by the scattering of the phonon D (D') mode and the impurity, gives D (D') peak at Raman shift similar to void-defective graphene.

An experimental study shows that $I(D)/I(D')$ can be used to distinguish the type of the defect on defective graphene in which sp^3 -defect if $I(D)/I(D') = 13$, and void-defect if $I(D)/I(D') = 7$ [59, 60]. Moreover, as shown in section 3.1, the eigenfrequencies can be determined using the dynamical matrix which is the second derivative of the potential. The potential reflects the interaction between atoms, so the alteration in bond length must cause the alteration in the eigenfrequencies. The variation of the C-C bond length nearby the defect typically broadens G peak which is C-C stretching mode. The experimental study, however, shows that the full width at half maximum (FWHM) of G peak changes insignificantly if N_D is low, but increases significantly if N_D is high [60].

There are two patterns of the edge of graphene which are zigzag and armchair edges. The translational symmetry is broken if the electron travels from the inside of the graphene sheet to the edge but preserved if the electron travels along the edge. Since zigzag and armchair edges have different geometry, the electron travels in reciprocal space in a different way. The former cannot travel from K to an intervalley K' which deactivates D peak but still activates D' peak, and the latter can travel from K to K' which activates both D and D' peaks (see Figure 4-2) [9]. The intensity of D peak activated by the armchair edge also strongly depends on polarization, in contrast to that activated sp^3 - and void-defects [61-63].

4.4 Vibrational analysis

The vibrational scheme of each phonon mode at Γ -point, obtained from the phonon eigenvector calculated using Equation (3.4), is used to analyze the Raman and/or IR active mode. The phonon mode is Raman-active (IR-active) when the polarization (dipole moment) in the unit cell changes during the vibration which can be analyzed through the point group of the crystal/molecule [64, 65]. Each vibrational mode changes the geometry of the crystal/molecule differently. If a set of atoms vibrates symmetrically (asymmetrically) through the principal axis of rotation and symmetrically through the rotation axis that perpendicular to the principal axis or vertical reflecting plane, that vibrational mode will be assigned to A_1 (B_1). But if the latter condition is an asymmetrical vibration, that vibrational mode will be assigned to A_2 (B_2). The letters E and F indicate to doubly and triply degenerate, respectively. For the structure that has a centrosymmetry, the subscripts g and u indicate to a set of atoms that vibrates symmetrically and asymmetrically, respectively, through the center of inversion, i (see Table 4-1). For the structure that has a horizontal plane of reflection, the superscripts prime and double prime indicate to a set of atoms that vibrates symmetrically and asymmetrically, respectively, through that plane, σ_h (see Table 4-2) [64].

The Raman and IR active/inactive mode can be read from the character tables by which the point group of the crystal structure is known. The character tables of point groups D_{3d} and D_{3h} are shown in Table 4-1 and Table 4-2, respectively, which will be used for the analysis in section 5.3. The first column in the character table shows the type of representations in which the phonon mode can be assigned to either one of this representation by considering the vibrational scheme. The last two columns in the character table present IR and Raman activities; the first column presents translational symmetry along x , y , and z axes (T_x , T_y , T_z) presenting IR active mode and rotational symmetry around x , y , and z axes (R_x , R_y , R_z), and the second column presents polarization product where α_{ij} is an element in the polarization matrix presenting Raman active mode.

Table 4-1 Characteristic table of point group D_{3d}

D_{3d}	E	$2S_6(z)$	$2S_6(z) \equiv 2C_3$	$S_6^3 \equiv S_2 \equiv i$	$3C_2$	$3\sigma_d$		
A_{1g}	+1	+1	+1	+1	+1	+1		$\alpha_{xx} + \alpha_{yy}, \alpha_{zz}$
A_{1u}	+1	-1	+1	-1	+1	-1		
A_{2g}	+1	+1	+1	+1	-1	-1	R_z	
A_{2u}	+1	-1	+1	-1	-1	+1	T_z	
E_g	+2	-1	-1	+2	0	0	(R_x, R_y)	$(\alpha_{xx} - \alpha_{yy}, \alpha_{xy}), (\alpha_{yz}, \alpha_{xz})$
E_u	+2	+1	-1	-2	0	0	(T_x, T_y)	

Table 4-2 Characteristic table of point group D_{3h}

D_{3h}	E	$2C_3(z)$	$3C_2$	σ_h	$2S_3$	$3\sigma_v$		
A'_1	+1	+1	+1	+1	+1	+1		$\alpha_{xx} + \alpha_{yy}, \alpha_{zz}$
A''_1	+1	-1	+1	-1	-1	-1		
A'_2	+1	+1	-1	+1	+1	-1	R_z	
A''_2	+1	+1	-1	-1	-1	+1	T_z	
E'	+2	-1	0	+2	-1	0	(T_x, T_y)	$(\alpha_{xx} - \alpha_{yy}, \alpha_{xy})$
E''	+2	-1	0	-2	+1	0	(R_x, R_y)	$(\alpha_{yz}, \alpha_{xz})$

5 Phase stabilities of hydrogenated BLG

A coating of BLG onto the substrate can enhance the hardness of its substrate [45]. However, to show the ultrahard effect, BLG must be indented to become a diamondized BLG first. In this chapter, a theoretical study using DFT shows that diamondized BLGs, which are diamondene and lonsdaleitene, can be stable without an indentation, but H atoms must be fully dangle on its two surfaces. Their vibrational analyses are performed to mark the possible Raman and IR active peaks for future experimental fabrication. The detail in this chapter is a part of the article in Ref. [48].

5.1 Overview

5.1.1 Crystal structure and energy contours

The path transformation between the diamondene and BLG is performed to seek for the possibility to create the diamondene. The diamondene, considered as a layer cut from a bulk diamond in [111] direction, has four C atoms in the unit cell. Its lattice parameter should be 2.52 Å, which is larger than 2.42 Å of BLG [10]. Moreover, the distance between C atoms on different layers of diamondene is 1.55 Å which is much smaller than 3.23 Å of BLG [10]. Three adjustments hence are required to transform from AB-stacked BLG to diamondene; 1) because the lattice parameter of diamondene is larger than that of AB-stacked BLG, so AB-stacked BLG must be stretched in in-plane direction, 2) because the interlayer distance of BLG is larger than that of diamondene, so it must be reduced, and 3) the angle C-C-C must be tilted in out-of-plane direction to form trigonal pyramidal shape.

Figure 5-1 shows the energy contours of the structural transformation between AB-stacked BLG and diamondene. The three adjustments are divided into several configurations with small steps (see Figure 5-1 (a)) where the energy of each step is obtained by *ab-initio* calculation. All contours in Figure 5-1 are plots of the energy difference with the energy of the configurations at step 0, 0% strain and 4 Å of the interlayer distance. For the flat BLG at step 0, the energy of BLG does not change when the interlayer distance is less than 2–4 Å but increases when the interlayer distance is less than ~2 Å. The increment of the energy is from Pauli's exclusion, causing repulsive force, of the overlapping between p_z -orbitals of two layers. In contrast, for the bent BLG in step 10, the energy of the system decreases when the interlayer distance is less than 2 Å and then increases when the interlayer distance is less than 1.5 Å. The strains up to -2% (compressive strain) and up to 5% (tensile strain), yielding ~2.51 Å which is an expected lattice parameter for diamondene, are applied to the system. Nevertheless, neither configurations have the energy lower than AB-stacked BLG. Thus, the diamondene could not be an energetically favorable phase without external auxiliaries [45, 47].

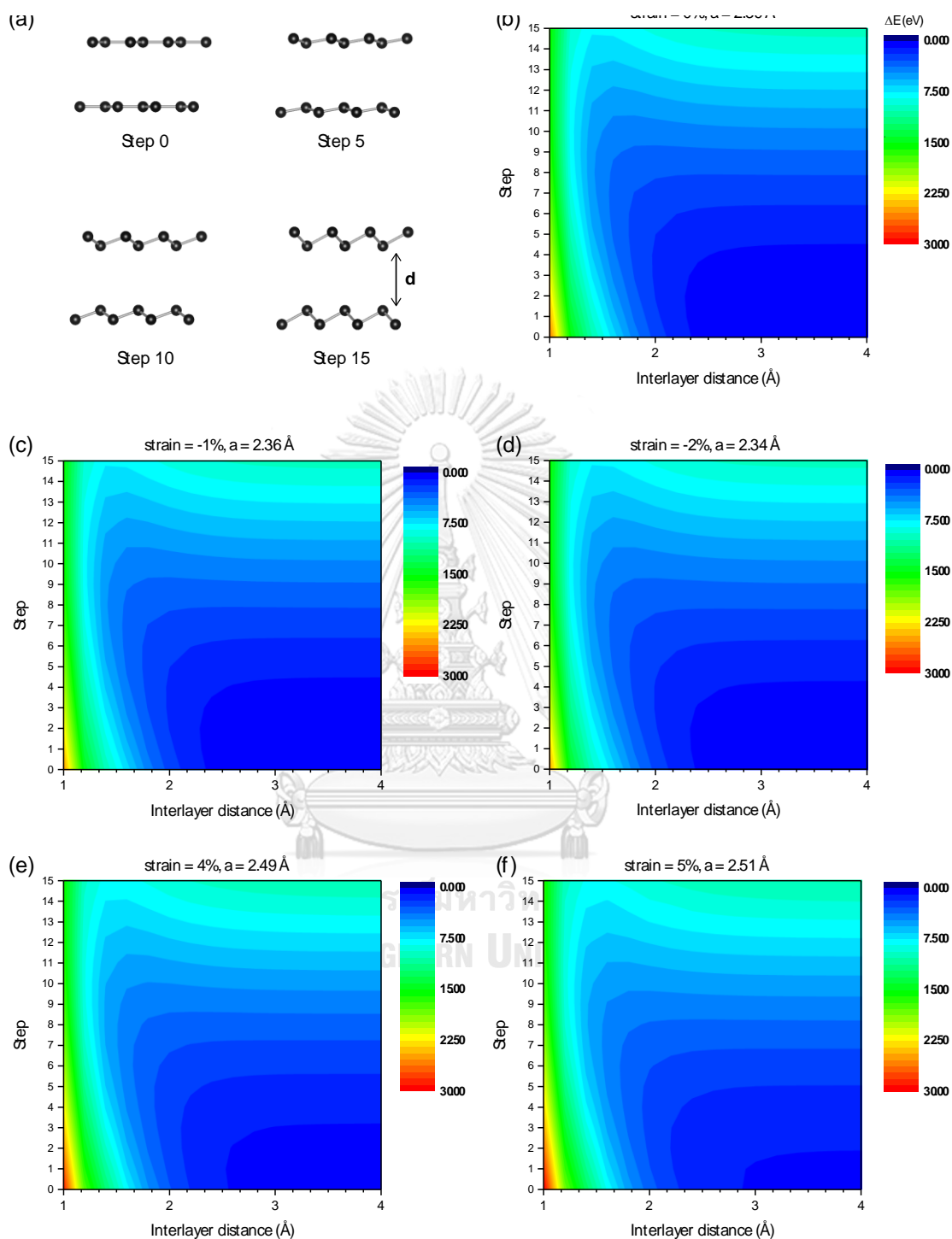


Figure 5-1 (a) The positions of C atoms are adjusted by altering the degree of bending between intralayer C atoms from flat layers at Step 0 to zigzag layers at Step 15, and d is the interlayer distance. (b) –(f) Contour plots of the energy landscape of 0%, -1%, -2%, +4%, and +5% strains, respectively, are illustrated the energy difference subtracted by the energy of BLG.

We introduce H atoms to passivate with lone-pair electrons of diamondene and lonsdaleitene surfaces which their chemical compositions change to C_4H_2 . Diamondene and lonsdaleitene, fully passivated by H atoms, are nomenclated as H-diamondene and H-lonsdaleitene, respectively. The structures of H-diamondene and H-lonsdaleitene are from AB-stacked BLG and AA-stacked BLG, respectively, which are different from the stacking sequence of the carbon sheets. Consequently, the point group of H-diamondene is D_{3d} in which the center of inversion is preserved, while the point group of H-lonsdaleitene is D_{3h} instead in which the horizontal mirror image is preserved.

The structural relaxations, performing on H-diamondene and H-lonsdaleitene, provide the equilibrium structural parameters at 0 K and 0 GPa, listed in Table 5-1. Two species of C atoms are C_C which is C atom connecting with other three C atoms and C_H which is C atom connecting with one H atom and other two C atoms. The lattice parameter, C_H - C_C , and C_C - C_C bond lengths of H-diamondene (H-lonsdaleitene) are 2.53 (2.52), 1.540 (1.538), and 1.560 (1.586) angstrom, respectively, similar to those of its bulk counterpart [66, 67]. The C_H -H bond lengths of 1.109 Å and 1.108 Å for H-diamondene and H-lonsdaleitene, respectively, are also similar to the C-H bond lengths of hydrocarbon molecules.

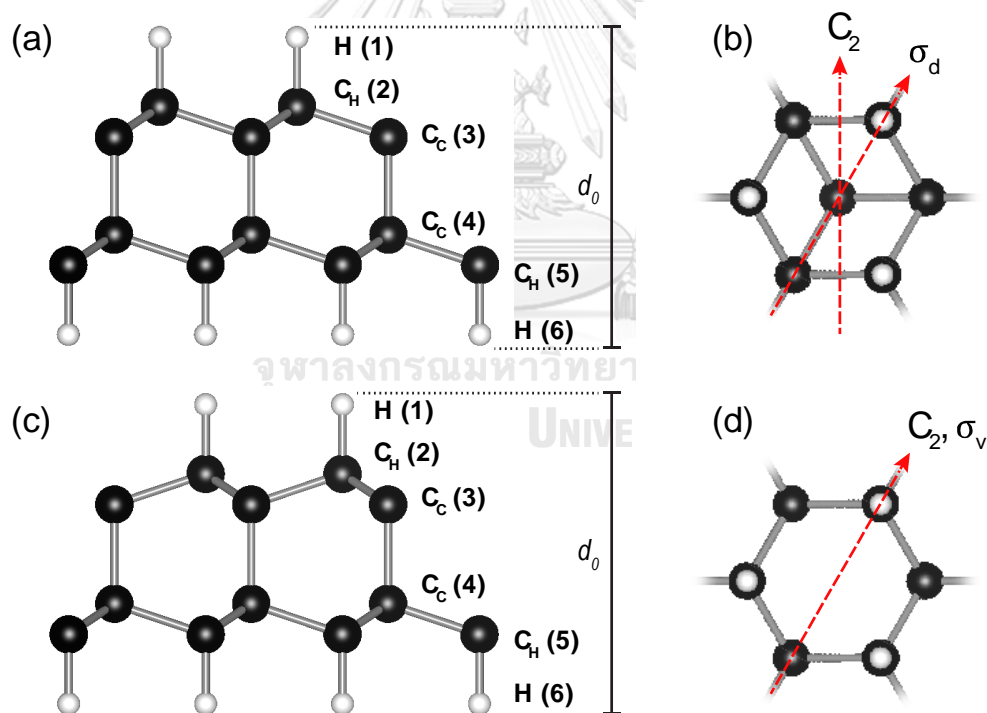


Figure 5-2 Crystal structures of (a)-(b) H-diamondene and (c)-(d) H-lonsdaleitene are presented in [001] direction directing upward for (a) and (c) and inward the page for (b) and (d). The numbers in parenthesis indicate the numbers of layers of the atom, and d_0 is the effective height. The red arrows show the direction of the rotation axis (C_2) and the mirror plane (σ).

Table 5-1 Relaxed positions of atoms in H-diamondene and H-lonsdaleitene with z fractionalized by 20 Å.

Atom	H-diamondene	H-lonsdaleitene
Space group	$P\bar{3}m1$	$P\bar{6}m2$
a (Å)	2.53	2.52
C_C	(0, 0, 0.038990)	(0, 0, 0.039664)
C_H	(1/3, 2/3, 0.063226)	(1/3, 2/3, 0.064190)
H	(1/3, 2/3, 0.11879)	(1/3, 2/3, 0.119595)

5.1.2 Electronic band structure

Figure 5-3 illustrates the electronic band structures of diamondized BLG comparing between with and without H dangling bonds. Since H-diamondene and H-lonsdaleitene have similar electronic band structures, the discussions of their electronic properties are wrapped together. Their electronic bands disperse across E_F , if there are no H atoms passivating with C atoms. We perform further analysis using the projected electronic density of states (DOS), which is the KS wavefunction projected onto the wavefunction of linear combination atomic orbital. The projected electronic DOS of diamondized BLG (without H atoms) shows that the electronic states around E_F are dominated by the electron in p_z -orbital of C_H atom which is left to be unbonded.

However, if H atoms are passivating on the surface of diamondized BLGs, the electron shells are filled opening the band gap widely which are 3.09 eV for H-diamondene and 2.87 eV for H-lonsdaleitene. The passivation of H atoms with the electron in p_z -orbital of C_H atom demolishes the unoccupied state of p_z -orbital near E_F causing the band gap opening. The states of p_x - and p_y -orbitals of C_C and C_H atoms then take place the valence states below E_F . The unoccupied state of p_z -orbital still dominates the conduction state but shift to higher energy. Hence, if the electron is excited from C_C and C_H atoms in the valence state to the p_z -orbital of C_H atom, it will travel through C_H atoms.

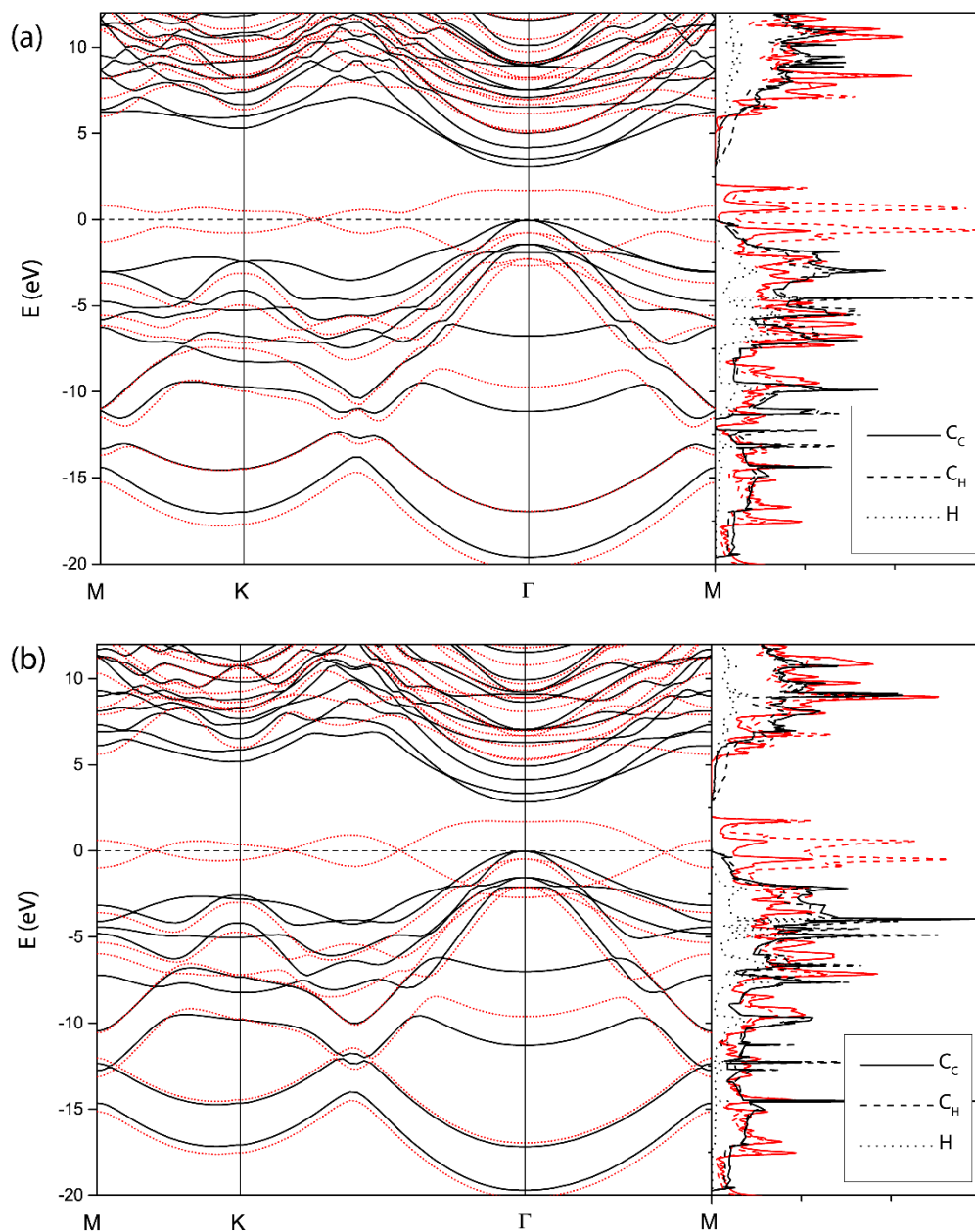


Figure 5-3 (a) (Left) Electronic band dispersions and (Right) electronic DOSs of H-diamondene (black lines) and diamondene (red lines). (b) (Left) Electronic band dispersions and (Right) electronic DOSs of H-lonsdaleitene (black lines) and lonsdaleitene (red dotted lines). For left figures, the solid, dashed, and dotted lines show electronic DOS of C_C , C_H , and H atoms, respectively.

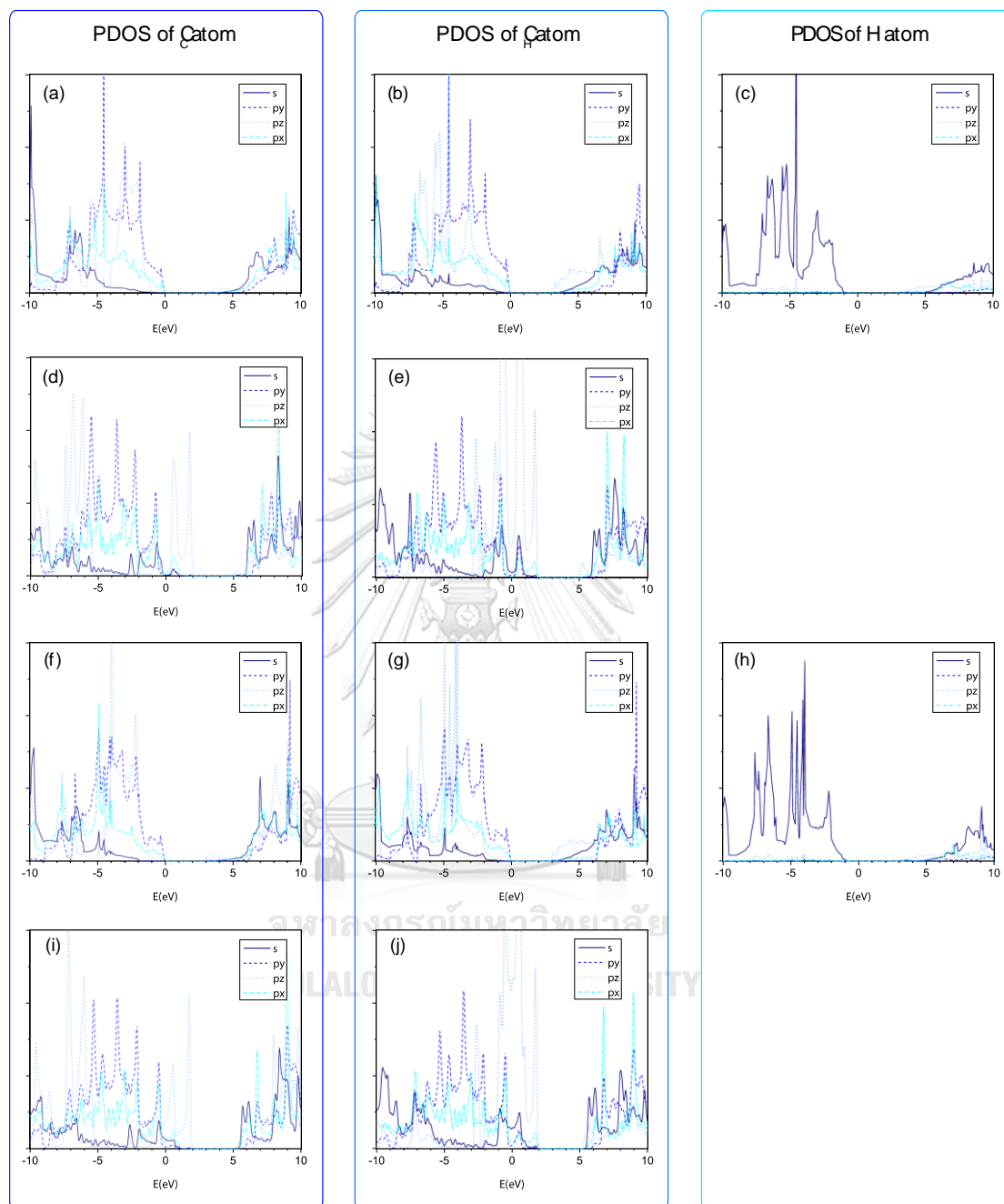


Figure 5-4 Projected electronic DOS of (a)-(c) H-diamondene, (d)-(e) diamondene, (f)-(h) H-lonsdaleitene, and (i)-(j) lonsdaleitene. The electronic DOS are projected onto s-orbital (solid line), p_x -orbital (dashed line), p_y -orbital (dotted line), and p_z -orbital (dash-dotted line). First, second and third columns are projected electronic DOS of C_C , C_H , and H atoms, respectively.

5.2 Phase stabilities

5.2.1 Thermodynamic stability

The formation energies of H-diamondene and H-lonsdaleitene, comparing with AB-stacked BLG and H₂ which are expected to be their precursors, are -13.66 and -3.97 meV, respectively. According to the condition in Equation (3.20), H-diamondene which has the lowest ΔG_{form} among all other phases in this study, so it is the most energetically favorable phase. However, if E_{zp} is included using Equation (3.19) at 0 K, the formation energies of H-diamondene and H-lonsdaleitene become positive values which indicate that the phonon tends to destabilize the structure of H-diamondene and H-lonsdaleitene. Their ΔG_{form} are even higher at a higher temperature (see Figure 5-5). Even though the energies of both phases are local minima in the energy landscape, so they can be stable if they exist in the first place.

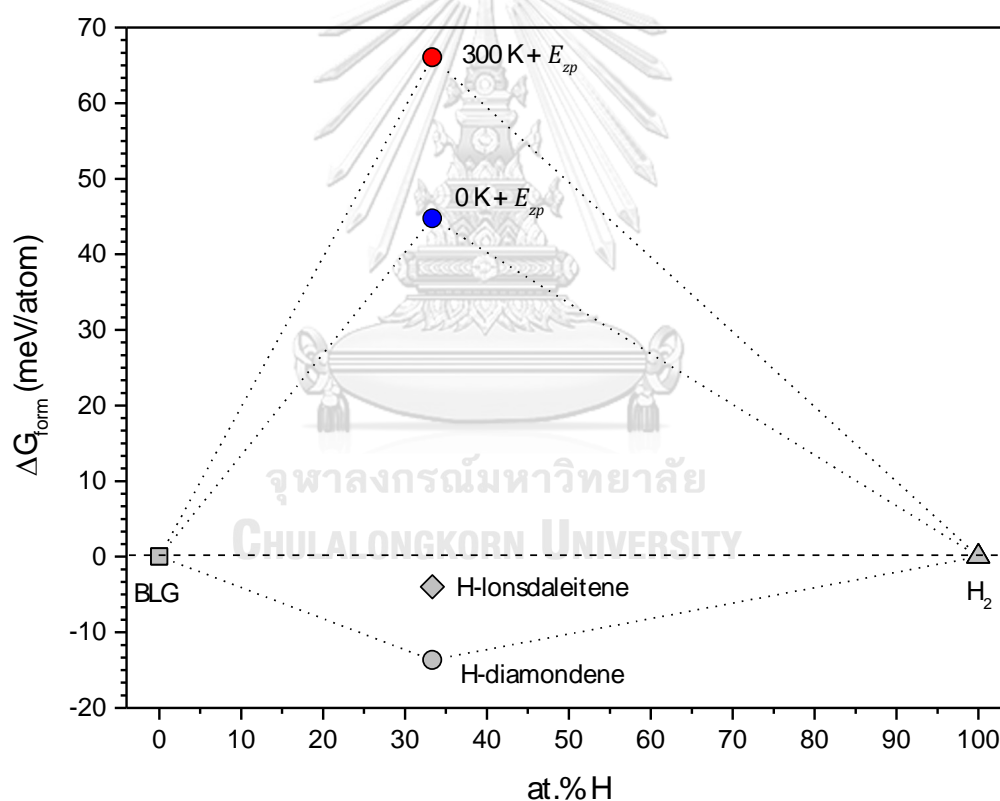


Figure 5-5 Convex hull shows Gibbs free energy of formation of H-diamondene (circle) and H-lonsdaleitene (diamond) using AB-stacked BLG (square) and H₂ molecule (triangle) as reactants/precursors. The energy part of the formation energy is calculated using only E_{int} and using Equation (3.11) at 0 K (blue symbol) and 300 K (red symbol).

5.2.2 Dynamical stability

Notwithstanding both H-diamondene and H-lonsdaleitene are thermodynamically destabilized by the phonon energy, they can be dynamical stable if the path of synthesis is found. Thus, the phonon dispersions of H-diamondene and H-lonsdaleitene are performed using harmonic approximation (see section 3.1). The Kohn anomaly at Γ -point and K-point, which is a characteristic of sp^2 -C in the phonon dispersion, disappears. The dispersion becomes dispersive like that of sp^3 -C. A new branch at $\sim 2900\text{ cm}^{-1}$ appears. It is from C-H stretching mode which will be discussed in the next section. The phonon dispersions in Figure 5-6 show no imaginary phonon modes except small extents around Γ -point. The degeneracy of three acoustic modes, which are two in-plane modes and one flexural (ZA) mode, is broken. The ZA mode is the out-of-plane vibration, and its branch is concave like other 2d materials. However, in the present work, small imaginary phonons of ZA mode come up leading to the dynamical instability of the system. Nevertheless, the small imaginary phonons may originate from the anharmonic effect.

We then employ the *ab-initio* molecular dynamics (AIMD) simulations to ensure that if H-diamondene and H-lonsdaleitene are stable phases. Their stability at temperature 300, 500, and 1000 K are investigated up to 10 ps which is at least 200 periods of vibration of C atoms. Figure 5-7 shows the formation energy and temperature of H-diamondene and H-lonsdaleitene oscillating with time which presents their dynamical stabilities up to 1000 K.

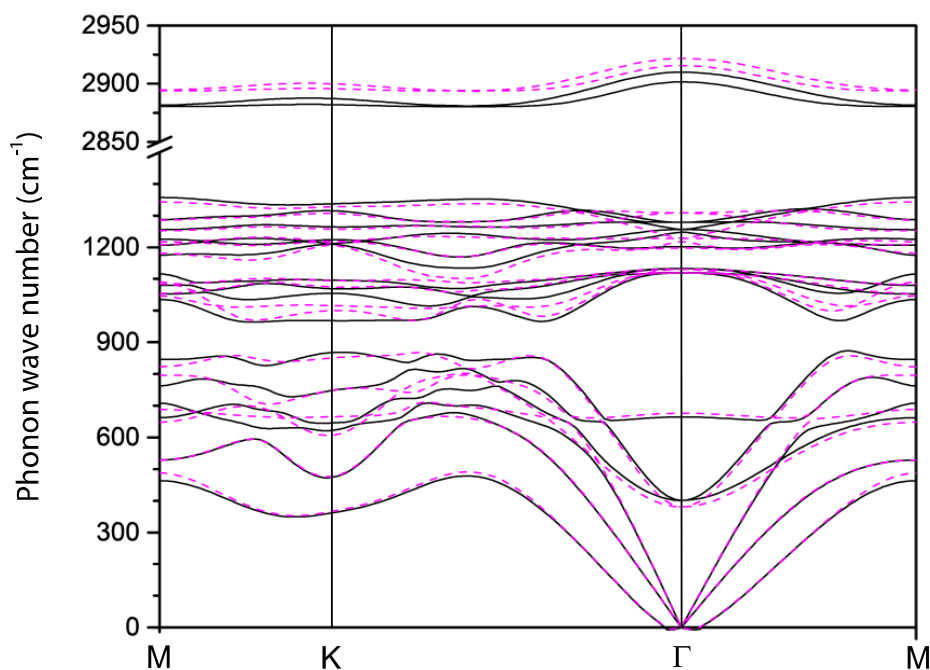


Figure 5-6 Phonon dispersions of H-diamondene (black line) and H-lonsdaleitene (pink dashed line).

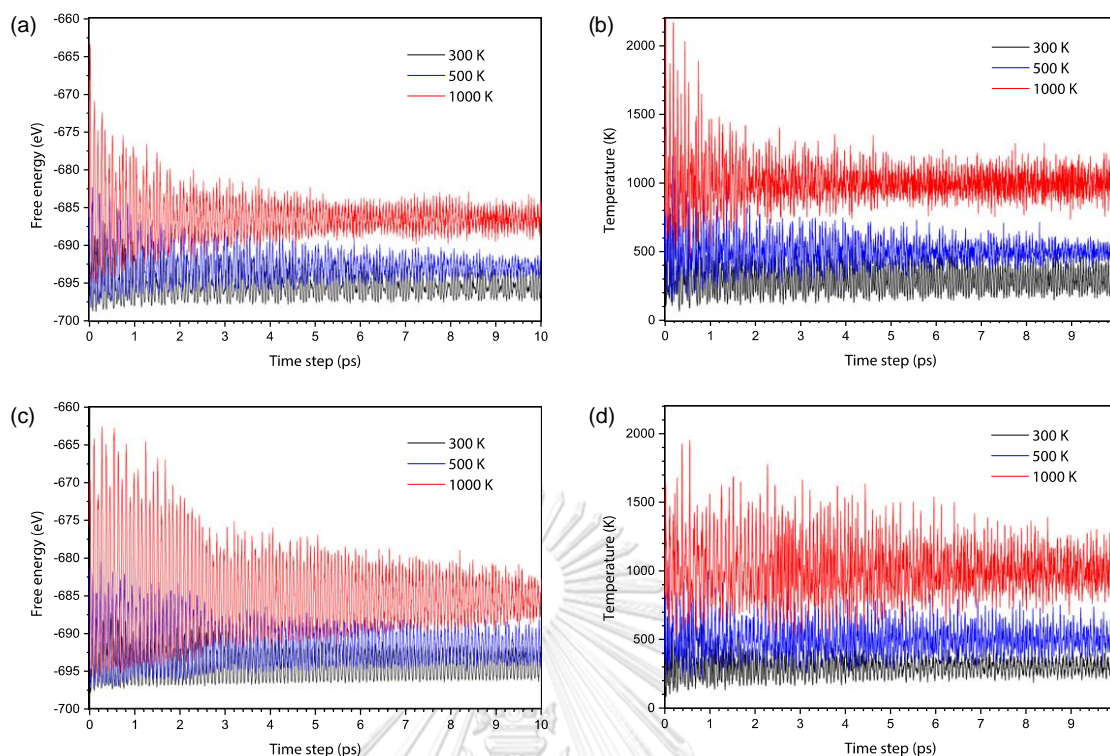


Figure 5-7 AIMD calculations up to 10 ps were performed to confirm the dynamical stability of H-diamondene and H-lonsdaleitene at 300 K (black line), 500 K (blue line), and 1000 K (red line). (a) Free energy and (b) temperature of H-diamondene. (c) Free energy and (d) temperature of H-lonsdaleitene.

5.3 Crystal vibration

5.3.1 Vibrational analysis

The Raman and IR spectroscopies are scientific tools used to characterize molecules and materials by detecting their vibrational frequencies. As discussed in section 4.1, Raman and IR spectra typically come from phonon around Γ -point, so the normal modes of H-diamondene and H-lonsdaleitene at Γ -point are analyzed and assigned to Raman and/or IR active/inactive as shown in Table 5-2 and Table 5-3.

Both H-diamondene and H-lonsdaleitene have 6 atoms that give 3 acoustic modes and 15 optical modes at Γ -point. Since the point group H-diamondene (H-lonsdaleitene) is D_{3d} (D_{3h}), the Raman active will be assigned to the modes that the vibration of the atoms preserves a center of inversion (a horizontal mirror plane) of the crystal structure. By the analysis of phonon eigenvectors, the vibrations of H-diamondene and H-lonsdaleitene can be divided into two characteristics; in-plane vibration assigned to non-degeneracy mode and out-of-plane vibration assigned to doubly-degeneracy mode (two modes with the same vibrational frequency, but different vibrational directions).

Table 5-2 Vibrational frequencies and their activity of H-diamondene at Γ -point.

Frequency (cm ⁻¹)	Vibrational mode	Activity
401.1	E _g	Raman
664.6	A _{1g}	Raman
1119.2	E _g	Raman
1132.9	E _u	IR
1202.2	A _{2u}	IR
1246.3	A _{1g}	Raman
1247.6	E _u	IR
1278.8	E _g	Raman
2901.6	A _{1g}	Raman
2909.9	A _{2u}	IR

Table 5-3 Vibrational frequencies and their activity of H-lonsdaleitene at Γ -point.

Frequency (cm ⁻¹)	Vibrational mode	Activity
380.4	E''	Raman
676.2	A' ₁	Raman
1118.5	E''	Raman
1130.4	E'	IR&Raman
1197.1	A'' ₂	IR
1218.1	A' ₁	Raman
1227.5	E'	IR&Raman
1308.7	E''	Raman
2915.7	A' ₁	Raman
2921.8	A'' ₂	IR

Table 5-4 Vibrational schemes of in-plane modes of H-diamondene with \rightarrow and \leftarrow symbols representing phase angle of vibration 180-degree difference.

Element (number of atomic layers arranged from top to bottom)	E_g	E_g	E_u	E_u	E_g
H (1)	→	→	→	→	→
C _H (2)	→	→	→	←	←
C _C (3)	→	←	←	→	→
C _C (4)	←	→	←	→	←
C _H (5)	←	←	→	←	→
H (6)	←	←	→	→	←

Table 5-5 Vibrational schemes of in-plane modes of H-lonsdaleitene with '→' and '←' symbols representing phase angle of vibration 180-degree difference and 'o' symbol representing non-vibration.

Element (number of atomic layers arranged from top to bottom)	E''	E'	E''	E'	E''
H (1)	→	→	→	→	→
C _H (2)	→	→	o	←	←
C _C (3)	→	←	←	→	→
C _C (4)	←	←	→	→	←
C _H (5)	←	→	o	←	→
H (6)	←	→	←	→	←

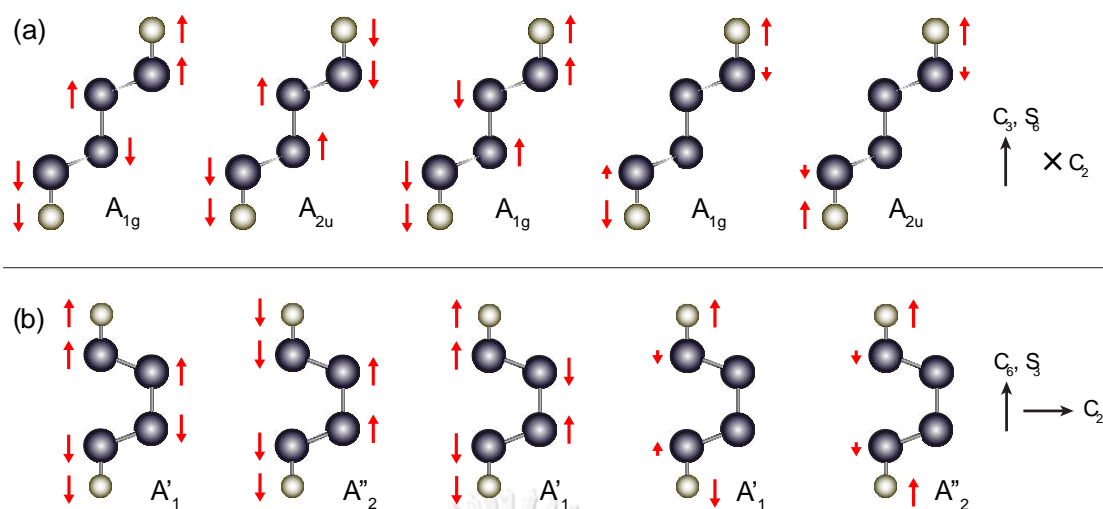


Figure 5-8 Vibrational schemes of (a) H-diamondene and (b) H-lonsdaleitene are presented from left to right by arranging from low to high frequencies as shown in Table 5-2 and Table 5-3, respectively. The arrows and cross show the direction of the rotation axis.

Diamondized hydrogenated BLGs exhibit 5 out-of-plane modes and 5 doubly degeneracy in-plane modes (10 vibrational modes in total) at Γ -point. For H-diamondene, three of five out-of-plane vibrational modes, which are A_{1g} mode at 665, 1248, and 2902 cm^{-1} , are Raman active and other two modes, which are A_{2u} mode at 1202, and 2910 cm^{-1} , are IR active. Three of five in-plane vibrational modes, which are E_g mode at 401, 1119, and 1279 cm^{-1} , are Raman active and the other two modes, which are E_u mode at 1133, and 1246 cm^{-1} , are IR active. For H-lonsdaleitene, three of five out-of-plane vibrational modes, which are A'_1 mode at 676, 1248, and 2902 cm^{-1} , are Raman active and other two modes, which are A''_2 mode at 1197, and 2922 cm^{-1} , are IR active. However, the optical activity of in-plane vibrational modes of H-lonsdaleitene is different from H-diamondene, even their vibrational schemes are alike. Two in-plane vibrational modes of H-lonsdaleitene, which are E' mode at 1130, and 1228 cm^{-1} , are both Raman and IR active and other three modes, which are E'' mode at 380, 1119, and 1309 cm^{-1} , are only Raman active.

5.3.2 Designation of vibrational schemes

The designation of vibrational schemes is beneficial in interpreting experimental results intuitively. We then start with out-of-plane modes whereby the vibrational schemes of H-diamondene and H-lonsdaleitene will be discussed simultaneously. The vibrational modes at $\sim 2900 \text{ cm}^{-1}$, which are two schemes from the left in Figure 5-8, exhibit H and C_H atoms vibrating out-of-phase (180-degree difference) in the out-of-plane direction. Thus, they can be assigned as a C-H stretching mode. The vibrational modes at ~ 670 and $\sim 1200 \text{ cm}^{-1}$, which are three schemes from the left in Figure 5-8, H and C_H atoms vibrating in-phase in the out-of-plane direction.

For the in-planes modes, the vibrational schemes are shown in Table 5-4 and Table 5-5. The vibrational modes at $\sim 1300 \text{ cm}^{-1}$, which are the leftmost schemes in

Table 5-4 and Table 5-5, H and C_H atoms vibrating out-of-phase in the in-plane direction. Thus, they can be assigned as C-H swaging mode. The vibrational modes at ~ 1100 and ~ 1300 cm^{-1} , which are second to fourth schemes in Table 5-4 and Table 5-5, H and C_H atoms vibrating in-phase but C_H and C_C atoms vibrating out-of-phase in the in-plane direction. If we depict the vibrational schemes of one of their degeneracy from a top view (see Figure 5-9 (a)), C atoms of hydrogenated diamondized BLGs vibrate analogously with the G mode of BLG which is C-C stretching mode [9]. The vibrational modes at ~ 400 cm^{-1} , which are the rightmost schemes in Table 5-4 and Table 5-5, present the atoms on the top three and bottom three atomic layers vibrating out-of-phase in the in-plane direction. The vibrational schemes, depicted in Figure 5-9 (b), present that C atoms of hydrogenated diamondized BLGs vibrate analogously with the shear mode of BLG [68].

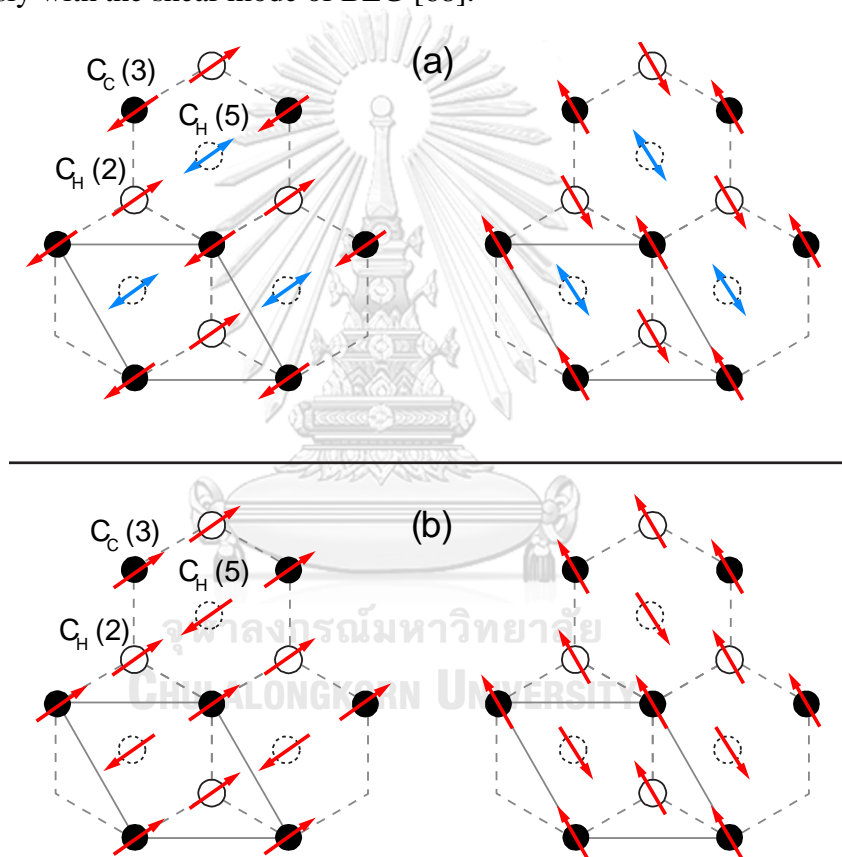


Figure 5-9 The in-plane vibrational schemes of (a) two degeneracy modes of the vibrational mode at ~ 1100 and ~ 1300 cm^{-1} and (b) two degeneracy modes of the vibrational mode at ~ 400 cm^{-1} are depicted. White and black balls present C atoms on second and third atomic layers, respectively, and dashed ball presents C atom at the fifth layer (see Table 5-4). Red and blue arrows point the motive direction of that atom at a certain time, but for blue arrow, an atom can move to either direction depending on the vibrational mode.

6 Phase stabilities of hydrogenated SLG

Hydrogenated SLG is a candidate for a spintronic application. The magnetization can be enhanced as long as H atoms bond with C atoms on A and B sites (see Figure 6-1 (a)) are not even [36]. However, the amount of H atoms on SLG is limited by phase instability. In the previous chapter, we discuss the phase stabilities of diamondized hydrogenated BLGs which are dynamically stable, but energetically unfavorable. Their Gibbs energies of formation become positive after the phonon energy has been included. For hydrogenated SLG, the experiment shows that partial hydrogenation is possible. Thus, in this chapter, the thermodynamic stability of hydrogenated SLGs with various H concentrations are studied. The phase stability as a function of strain, which is beneficial for future fabrication, will be discussed.

6.1 Overview

In the study, the H concentration of hydrogenated SLG is varied by increasing the unit cell of SLG from 2 to 98 C atoms where a number of H atom per unit cell is kept to be one (see Figure 6-2). This ensures that H atoms are on the same site (A or B) in an infinite space which maximizes the magnetization and deposited on one side of SLG. For two-sided hydrogenated SLG, C_6H_5 and $C_{18}H_{17}$, which one of H atom per unit cell is absence, are studied for comparison with one-sided hydrogenated SLG.

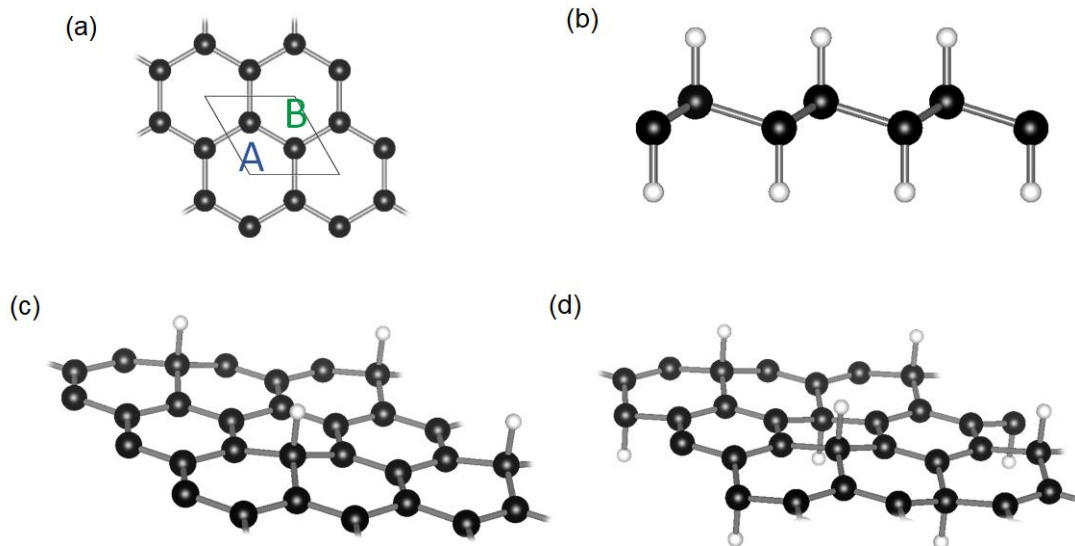


Figure 6-1 (a) Hexagonal net of SLG labeled by A and B sites presenting two different in a unit cell (black rhombus). (b) Structure of graphene. (c) One-sided hydrogenated SLG. (d) Two-sided hydrogenated SLG.

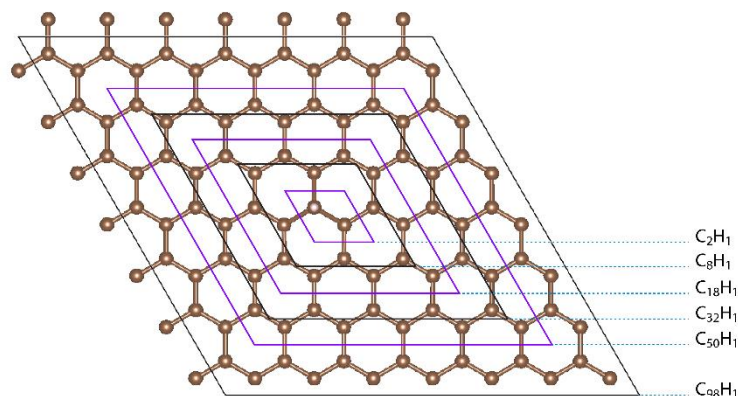


Figure 6-2 Various sizes of rhombus present the unit cells of C_2H_1 , C_8H_1 , $C_{18}H_1$, $C_{32}H_1$, $C_{50}H_1$, and $C_{98}H_1$.

6.2 Thermodynamic stability

The Gibbs free energies of formation of various hydrogenated SLGs are plotted in Figure 6-3 with respect to $n/(m+n)$ of C_mH_n . All one-sided hydrogenated SLGs ($0 < n \leq 1/3$) have positive formation energies, therefore, none of one-sided hydrogenated SLG are energetically favorable. In contrast, the formation energy of graphane (C_2H_2) is -137.4 meV/atom and increases to -58.32 and -31.03 meV/atom at 0 and 300 K, respectively, if the phonon energy is included. The result of graphane is contrary to diamondized hydrogenated BLGs since they are thermodynamically destabilized at 300 K. Even though the formation energy of graphane at 300 K is larger than thermal energy (~ 25 meV), the experiment cannot successfully synthesize it.

It is worth noting that the van der Waals interaction, DFT-D3 or zero damping method of Grimme, is included in the *ab-initio* calculations of all structures in Chapter 6. However, the energies used to evaluate the convex hull in Chapter 5 are not calculated by including the van der Waals interaction. We found that the calculated energies with including the van de Waals interaction are much lower than without including it for the fully hydrogenating cases such as graphane and H-diamondene. The reason is that two H atoms interact with each other by van de Waals force if they are depositing on the neighboring C atoms. Therefore, the van der Waals interaction is largest when H atoms fully arranging on C atoms. Nevertheless, the result in Chapter 5 does not change even the van der Waals interaction has been included.

Furthermore, the strain of graphene can be controlled by piezo substrate [17]. The strain could cause the phase transition in 2d materials. The stabilities of hydrogenated SLGs with tensile and compressive strains are studied up to 15% strain. Figure 6-4 shows the Gibbs free energy of the formation of hydrogenated SLG under various strains. For graphane, its ΔG_{form} decreases from -31.03 meV/atom for zero strain to -124.2 and -162.1 meV/atom for 10% tensile strain and 10% compressive strain,

respectively. For one-sided hydrogenated SLGs, their ΔG_{form} are decreased by the influence of both tensile and compressive strains. Nevertheless, they are positive values, so none of the one-sided hydrogenated SLGs are energetically favorable at any cause of strains (see Figure 6-4). In an exception, the structure of $C_{18}H_1$ with 10% compressive strain is corrugated making its ΔG_{form} a negative value (see Figure 6-4).

The strain can enhance the phase stability of graphene by lowering its formation energy. This result may help the experiment to find the technique to synthesize graphene. Some of one-sided hydrogenated SLGs can be energetically favorable phase, but highly compressive strain must be applied.

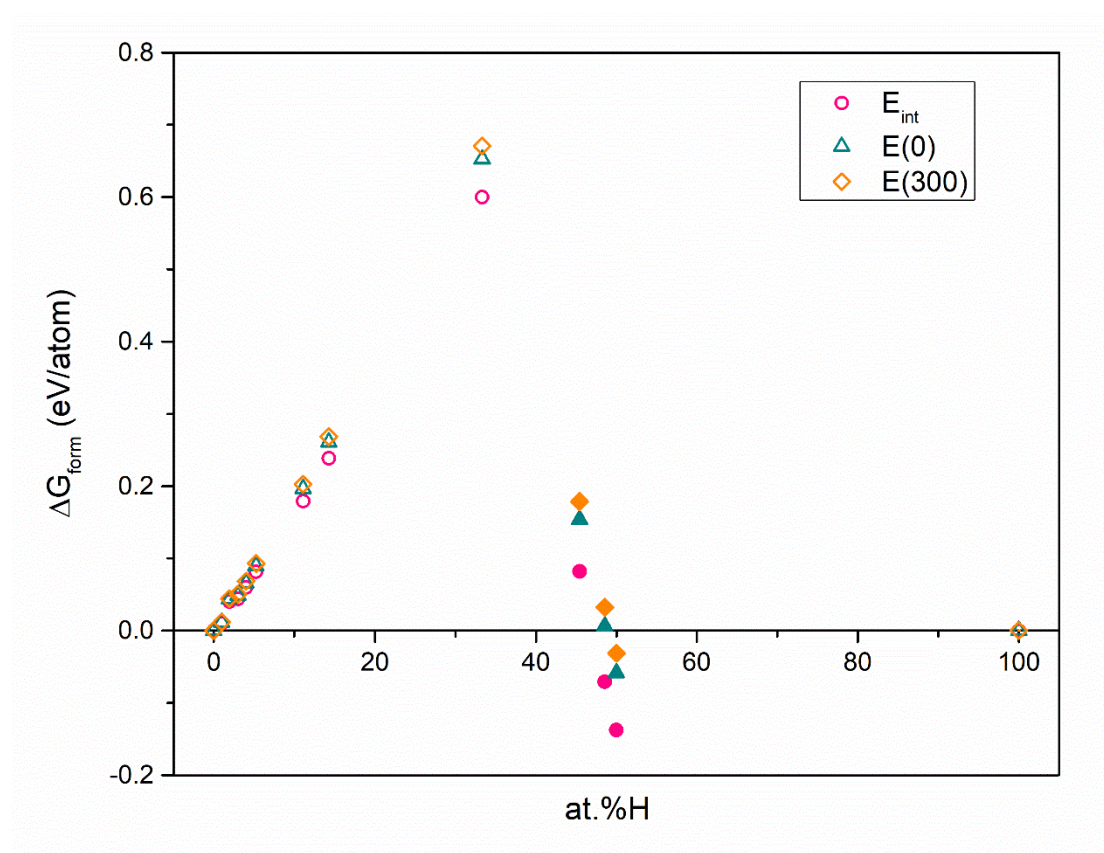


Figure 6-3 Convex hull shows Gibbs free energy of formation of hydrogenated SLG containing various H concentrations. The energy part of the formation energy is calculated using only E_{int} (circle) and using Equation (3.11) at 0 K (triangle) and 300 K (diamond symbol). The opened and solid symbols represent one-sided hydrogenated SLG and two-sided hydrogenated SLG, respectively.

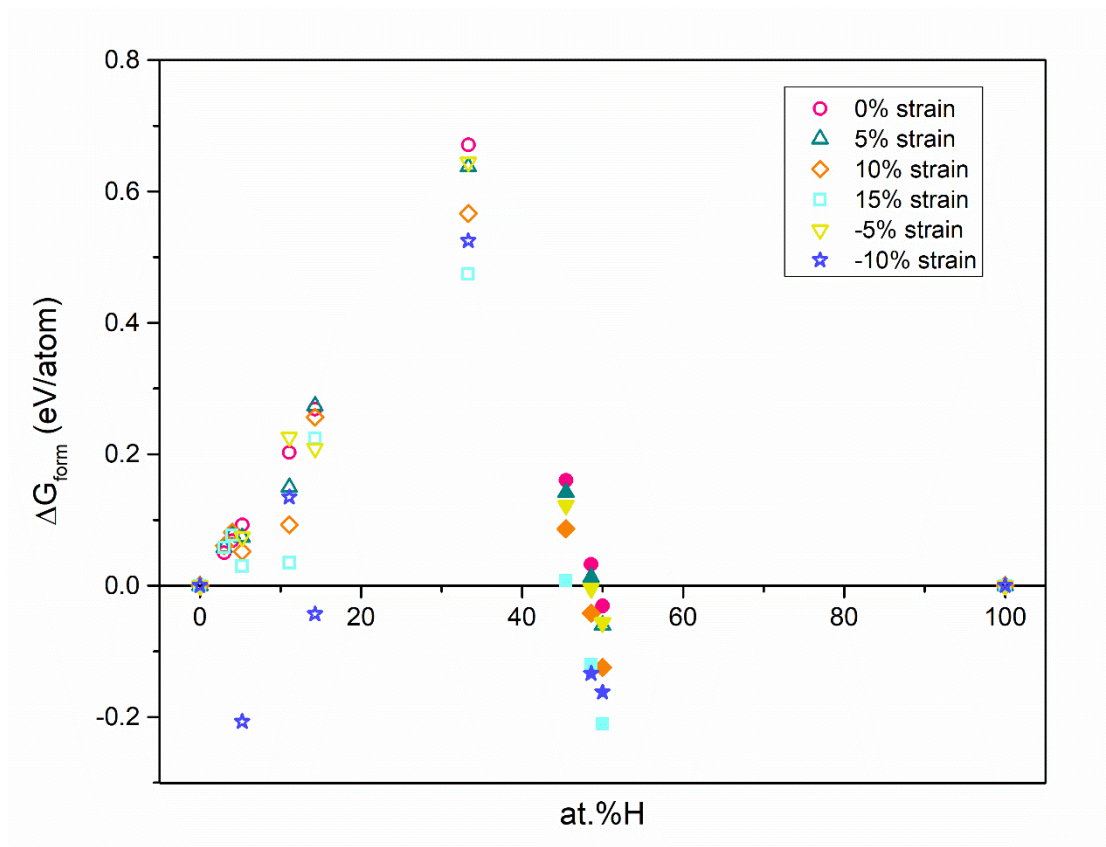


Figure 6-4 Convex hull shows Gibbs free energy of formation of hydrogenated SLG containing various H concentrations at 300 K. The opened and solid symbols represent one-sided hydrogenated SLG and two-sided hydrogenated SLG, respectively.

7 Slipping Model

In this chapter, we present a mathematical approach for an ultrathin film, *i.e.*, SLG, slipping from its substrate under compression [21]. The film and the substrate compressed by the same pressure will have different strains which means that the film slips from the substrate because their elastic constants are different. However, the film is held with the substrate by van de Waals force causing the frictional stress between two surfaces. Herein, the derivations of the coefficient of frictional stress and total stress acting on the film are presented. In the pristine sample, an area of the substrate surface is preliminarily presumed to be equal to an area of the film,

$$A_{sub}(0) = xA_{film}(0), \quad (7.1)$$

where $A_{sub}(P)$ and $A_{film}(P)$ are the area of the substrate surface per unit cell and the area of the film per unit cell at pressure, P , respectively, and x is a number of the unit cell of the film that fully fills the unit cell area of the substrate. Then

$$A_{sub}(P) - A_{sub}(0) = x[A_{film}(P) - A_{film}(0)], \quad (7.2)$$

Combining Equations (7.1) and (7.2),

$$\frac{\Delta A_{sub}}{A_{sub}(0)} = \frac{\Delta A_{film}}{A_{film}(0)}, \quad (7.3)$$

where $\Delta A_{sub} = A_{sub}(P) - A_{sub}(0)$ and $\Delta A_{film} = A_{film}(P) - A_{film}(0)$. The condition in Equation (7.3) may not be satisfied if the film and the substrate have different elastic constants. Therefore,

$$\frac{\Delta A_{sub}}{A_{sub}(0)} = \eta_i \frac{\Delta A_{film}}{A_{film}(0)}, \quad (7.4)$$

where η_i is added to take into account the case of the film slipping from the substrate deforms more than the Cu contact area.

In the experiment, the film and the substrate are in the same *in situ* which has an isotropic pressure,

$$P = \begin{bmatrix} \sigma_{ext} & 0 & 0 \\ 0 & \sigma_{ext} & 0 \\ 0 & 0 & \sigma_{ext} \end{bmatrix}, \quad (7.5)$$

where σ_{ext} is an external stress. The frictional stress is constructed as

$$\alpha_i \sigma_{sub-film}, \quad (7.6)$$

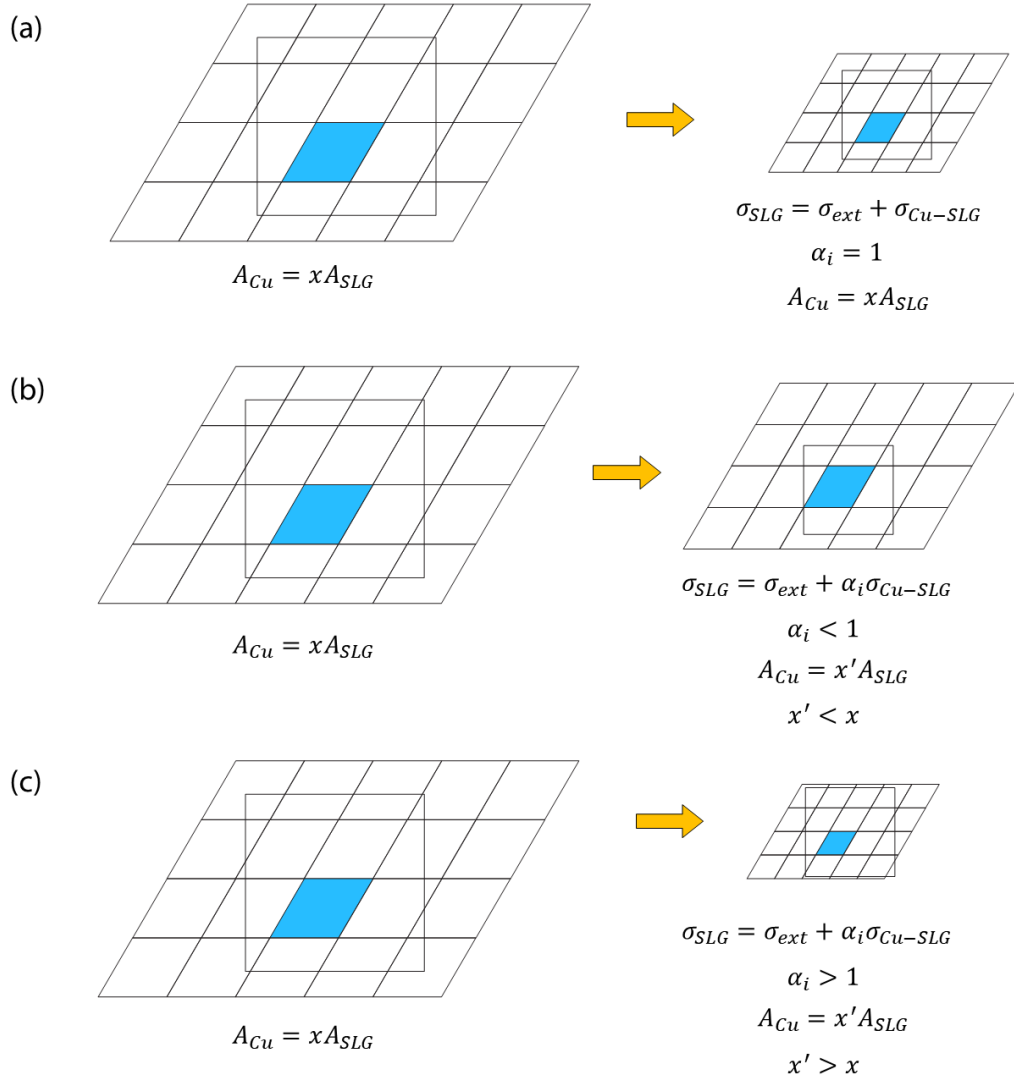


Figure 7-1 Schematic deformation of SLG on Cu substrate; (a) SLG area and Cu contact area deform equally, (b) SLG area deforms less than Cu contact area, and (c) SLG area deforms more than Cu contact area.

where α_i is a coefficient of frictional stress, and $\sigma_{sub-film}$ is a frictional stress from the substrate acting on the film. Therefore, the total stress acting on the film is

$$\sigma_{film} = \sigma_{ext} + \alpha_i \sigma_{sub-film}. \quad (7.7)$$

Because the film is not compressed by just pressure, but by the total stress, so the area of the film per unit cell under high pressure will be

$$A_{film}(P) \rightarrow A_{film}(\sigma_{film}) \quad (7.8)$$

We can express a function in Equation (7.8) into a linear equation to obtain the fitting parameter,

$$\frac{\Delta A_{film}}{A_{film}(0)} = \frac{A_{film}(\sigma_{film}) - A_{film}(0)}{A_{film}(0)} = \lambda_{film} \sigma_{film}, \quad (7.9)$$

where λ_{film} is a fitting parameter of the film.

For SLG, we can determine $\frac{\Delta A_{film}}{A_{film}(0)}$ using the relation between strain and ω_G , which can be obtained from the experiment,

$$\varepsilon(\omega_G) = -\frac{1}{(1-\nu)\gamma_G} \left(\frac{\omega_G - \omega_G^0}{\omega_G^0} \right), \quad (7.10)$$

where ν is a Poisson's ratio, 0.167, ω_G^0 is a frequency of G peak of SLG at 0% strain, and γ_G is a Grüneisen parameter of phonon G mode. The value of ω_G^0 is 1583 cm^{-1} obtained from the average data of pristine SLG on Cu substrate of Run 1 (see Chapter 8). Since a range of values have been reported for γ_G [17, 18, 44], we use the data from Ref. [21] which are from high-pressure experiments of SLG on a diamond substrate, to calculate γ_G by [69]

$$\frac{\omega_G - \omega_G^0}{\omega_G^0} = \frac{\gamma_G}{3Y(1-2\nu)} \Delta P, \quad (7.11)$$

where Y is Young's modulus which is more meaningful for 2-dimensional materials. The fitting results of γ_G and Y are 1.90 and 1.5 TPa, respectively, which are similar to the results of other experiments [17, 18, 44]. The list of fitting parameters and reference data are shown in Table 7-1. The area of strained SLG per unit cell can be calculated by

$$\frac{\Delta A_{film}}{A_{film}(0)} = \left(\frac{a_{SLG}(\varepsilon)}{a_{SLG}(0)} \right)^2 - 1 = 2\varepsilon(\omega_G) + \varepsilon^2(\omega_G), \quad (7.12)$$

Combining Equation (7.10) and (7.12), then

$$\frac{\Delta A_{film}}{A_{film}(0)} = -2\beta\Delta\omega_G + \beta^2\Delta\omega_G^2 \quad (7.13)$$

where $\beta = \frac{1}{\omega_G^0(1-\nu)\gamma_G}$. Therefore, we can obtain the fitting parameter of SLG by

$$-2\beta\Delta\omega_G + \beta^2\Delta\omega_G^2 = \lambda_{film}\sigma_{film} \quad (7.14)$$

It is difficult to determine σ_{film} from the experiment. Graphite is a stacking of SLG, so under compression, each layer of graphite should shrink simultaneously and equally. Therefore, the frictional stress between layers is likely very small and can be neglected. Bousige *et al.* [21] demonstrates that $\frac{\partial\omega_G}{\partial P}$ of SLG on diamond substrate is similar to that of graphite.

$$-2\beta\Delta\omega_G + \beta^2\Delta\omega_G^2 = \lambda_{film}P \quad (7.15)$$

Then, we fit Equation (7.15) with the data of SLG on the diamond substrate from Ref. [21] to obtain λ_{film} . From the parameter λ_{film} , we can calculate total stress acting on SLG, which can be applied on any substrate, using the Equation (7.14)

$$\sigma_{film} = \frac{-2\beta\Delta\omega_G + \beta^2\Delta\omega_G^2}{\lambda_{film}} \quad (7.16)$$

Furthermore, the Cu substrate is subjected by the external stress, so the area of Cu per unit cell under high pressure will be

$$A_{sub}(P) \rightarrow A_{sub}(\sigma_{ext}) \quad (7.17)$$

We can express a function in Equation (7.16) into a quadratic equation to obtain the fitting parameter

$$\frac{\Delta A_{sub}}{A_{sub}(0)} = \frac{A_{sub}(\sigma_{ext}) - A_{sub}(0)}{A_{sub}(0)} = \lambda_{sub_1}\sigma_{ext} + \lambda_{sub_2}\sigma_{ext}^2 \quad (7.18)$$

where λ_{sub_1} and λ_{sub_2} are fitting parameters of the substrate. And

$$\frac{\Delta A_{sub}}{A_{sub}(0)} = \left(\frac{V_{sub}(P)}{V_{sub}(0)}\right)^{2/3} - 1, \quad (7.19)$$

Combining Equation (7.17) and (7.18), then

$$\left(\frac{V_{sub}(P)}{V_{sub}(0)}\right)^{2/3} - 1 = \lambda_{sub_1}\sigma_{ext} + \lambda_{sub_2}\sigma_{ext}^2, \quad (7.20)$$

and, we fit Equation (7.18) with the data from Ref. [70] to obtain λ_{sub_1} and λ_{sub_2} (see Table 7-1).

Hereby, combining Equation (7.7), (7.9) and (7.17), then

$$\lambda_{sub_1}\sigma_{ext} + \lambda_{sub_2}\sigma_{ext}^2 = \eta_i\lambda_{film}(\sigma_{ext} + \alpha_i\sigma_{sub-film}) \quad (7.21)$$

$$\alpha_i\sigma_{sub-film} = \left(\frac{\lambda_{film_1}}{\eta_i\lambda_{film}} - 1\right)\sigma_{ext} + \left(\frac{\lambda_{sub_2}}{\eta_i\lambda_{film}}\right)\sigma_{ext}^2. \quad (7.22)$$

We set a condition that if $\alpha_i = 1$, $\eta_i = 1$, then

$$\sigma_{sub-film} = \left(\frac{\lambda_{sub_1}}{\lambda_{film}} - 1\right)\sigma_{ext} + \left(\frac{\lambda_{sub_2}}{\lambda_{film}}\right)\sigma_{ext}^2. \quad (7.23)$$

Combining Equation (7.21) and (7.22), then

$$\alpha_i = \frac{1}{\eta_i} \left[\frac{(\lambda_{sub_1} - \eta_i \lambda_{film}) \sigma_{ext} + \lambda_{sub_2} \sigma_{ext}^2}{(\lambda_{sub_1} - \lambda_{film}) \sigma_{ext} + \lambda_{sub_2} \sigma_{ext}^2} \right], \quad (7.24)$$

or

$$\alpha_i = \left[\frac{\lambda_{film}}{(\lambda_{sub_1} - \lambda_{film}) \sigma_{ext} + \lambda_{sub_2} \sigma_{ext}^2} \right] (\sigma_{film} - \sigma_{ext}), \quad (7.25)$$

Table 7-1 List of parameters used for fitting data in the present work.

	λ_{Cu_1} (GPa ⁻¹)	λ_{Cu_2} (GPa ⁻¹)	λ_{SLG} (GPa ⁻¹)	γ_G	Y (TPa)
This work	-0.0054 ^a	7×10^{-5}	-0.003	1.90	1.5
Ref. [17]				1.99	
Ref. [18]				1.86	
Ref. [44]					1.0

8 Hydrogenation pathway of hydrogenated SLG at high pressure

In this chapter, we perform the experiment to study the thermodynamic pathway, which considers temperature and pressure as a cause of the chemical reaction, of the hydrogenated SLG. A laser is used to heat SLG on a Cu substrate under pressure up to 20 GPa, and the chemical change is examined by Raman spectroscopy after the sample cooled to room temperature. The interpretation of Raman spectra will be given to confirm the creation of highly hydrogenated SLG at high pressure. It is worth noting that the detail in this chapter is a part of the article in Ref. [71].

8.1 Experimental procedures

In this study, the diamond anvil cell (DAC) is a choice of devices in order to create pressure such several gigapascals. The advantage of this technique is that the spectroscopy technique can be used to probe the alteration of the structures and/or the chemistry of the sample inside DAC. Figure 8-1 is a symmetric DAC with two pieces assembling (Right); cylinder (Left) and piston (Center). Two diamonds with $\sim 300 \mu\text{m}$ diameter of a culet, glued with epoxy to suspend on tungsten carbide seeds, are set at the centers of the piston and the cylinder. A direct contact between two diamonds can damage their culets, so the gasket made of Re is set in-between the diamonds.

To create a high-pressure cavity for the sample to sit on the diamond, the Re gasket was indented to $\sim 37\text{-}45 \mu\text{m}$ thickness by two diamonds and drilled a hole with $\sim 190 \mu\text{m}$ diameter at the center by a laser. The pressure can be generated by gently screwing after the sample and PTM all set inside the cavity.

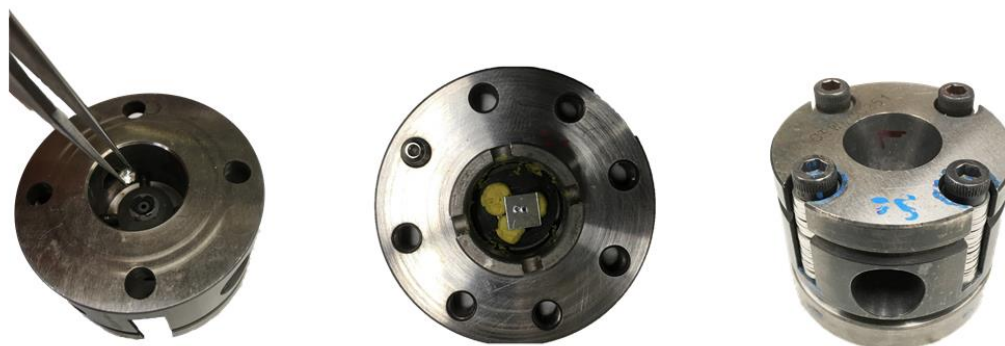


Figure 8-1 Symmetric diamond anvil cell; (Left) Cylindrical side with a diamond and its seed, (Center) Piston side with indented Re gasket, and (Right) Compact cell prompting to pressurize the sample by screwing.



Figure 8-2 (Left) CVD SLG on Cu foil from Graphenea, and (Right) Cut sample magnified by the microscope.

The sample used in this study is a SLG grown on a $\sim 18 \mu\text{m}$ thick Cu substrate by chemical vapor deposition (CVD) technique from the Graphenea company. It is cut into pieces smaller than $70 \times 70 \mu\text{m}^2$ with a razor blade (Figure 8-2 (Right)) and moved to the cavity by a tweezer. KCl dried at $120 \text{ }^\circ\text{C}$ with $\sim 3\text{-}5 \mu\text{m}$ thickness is in-between SLG/Cu and the diamond culet to be a thermal insulator preventing the heat dissipating through diamond immensely during the laser-heating (see Figure 8-3). Research grade hydrogen and helium gases (99.999% purity) are used as PTM and/or reactants in separate experiments. A continuous 1065 nm laser with 10 nm linewidth FWHM was used for one-side laser-heating by focusing on KCl/Cu.

We perform three experiments which are named as Run 1, Run 2 and Run 3. For Runs 1 and 2, H_2 PTM is used for the chemical reactant, and the laser-heating is performed at 8 and 20 GPa, respectively. For Run 3, He PTM is used as a control run, and the laser-heating is performed at 8 GPa. In Run 1, the sample is laser-heated for 3 times, while in Runs 2 and 3, the samples are laser-heated 2 times. The laser power is sequentially increased to heat the sample.

A CCD camera with near IR sensitivity continuously monitored the heating process, and spectroradiometric temperature measurements were collected at discrete times. Raman spectra at high pressures [72] and of the recovered samples were recorded using a single-frequency solid-state laser with a wavelength of 488 nm and a single-stage grating spectrograph equipped with a CCD detector. The spectral resolution was 4 cm^{-1} when using a grating of 1500 grooves/mm. A custom-built confocal Raman microscope collected the signal in a back-scattering geometry using a Mitutoyo 20X, $\text{NA}=0.4$ objective lens; ultra-low frequency holographic solid-state notch filters allowed measurement of the spectra down to 10 cm^{-1} . The pressure was measured using the ruby fluorescence scale.

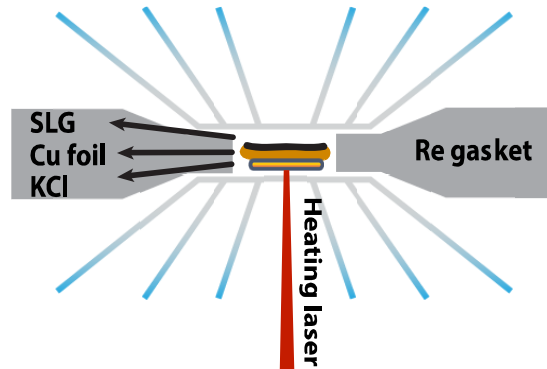


Figure 8-3 The experimental setup for this work.

8.2 Ruby pressure gauge

A direct method of pressure measurement is impracticable with the DAC technique since a force acting on an area of sample cannot be determined. Therefore, the pressure measurement using ruby fluorescence was introduced by Mao *et al.* [73] which is very powerful for the sample inside the *in situ*. The pressure can be determined by

$$P = \frac{A}{B} \left[\left(1 + \frac{\Delta\lambda}{\lambda_0} \right)^B - 1 \right] \quad (8.1)$$

where λ_0 is a wavelength of Ruby fluorescence at 1 atm, $\Delta\lambda$ is a changing of Ruby fluorescence at high pressure, A and B are fitting parameters. Equation (8.1) was fitted with the pressure determined from the volumes of several metals in which their equations of state were known.

In the present experiment, pieces of ruby powder are put inside the high-pressure cavity together with the sample for pressure determination. The fluorescence of ruby is measured by a 532 nm laser and the fitting parameters are taken from Ref. [74] for pressure calculation.

8.3 Temperature estimation

During the third laser-heating in Run 1, we noticed a strong visible light emission from the heated spot. An optical micrograph in Figure 8-4 shows that KCl and Cu around the heated spot melted, but the SLG side did not alter as observed visually. At 10 GPa, the melting points of Cu and KCl are ~ 1600 K [75] and ~ 2300 K [76], respectively, so the achieved temperature of the third laser-heating in Run 1 is estimated to be about 2300 K or over. However, the temperature on the SLG side must be colder than the KCl side. The heat spreading from the heated spot mostly dissipates through the diamond, since it has very high (interfacial) thermal conductivity. KCl is used to separate the heated spot which is at a backside of the sample from the diamond. However, the amount of heat that reaches the SLG side is still less than at the heated spot even in a steady state.

We evaluate the temperature at the SLG based on the results of finite element calculations, which use the realistic geometric and thermochemical parameters [77], and plot as a contour in Figure 8-5. We estimate the highest temperature at the SLG to be below 1200 K and slightly lower in the area radially far from the heated spot.

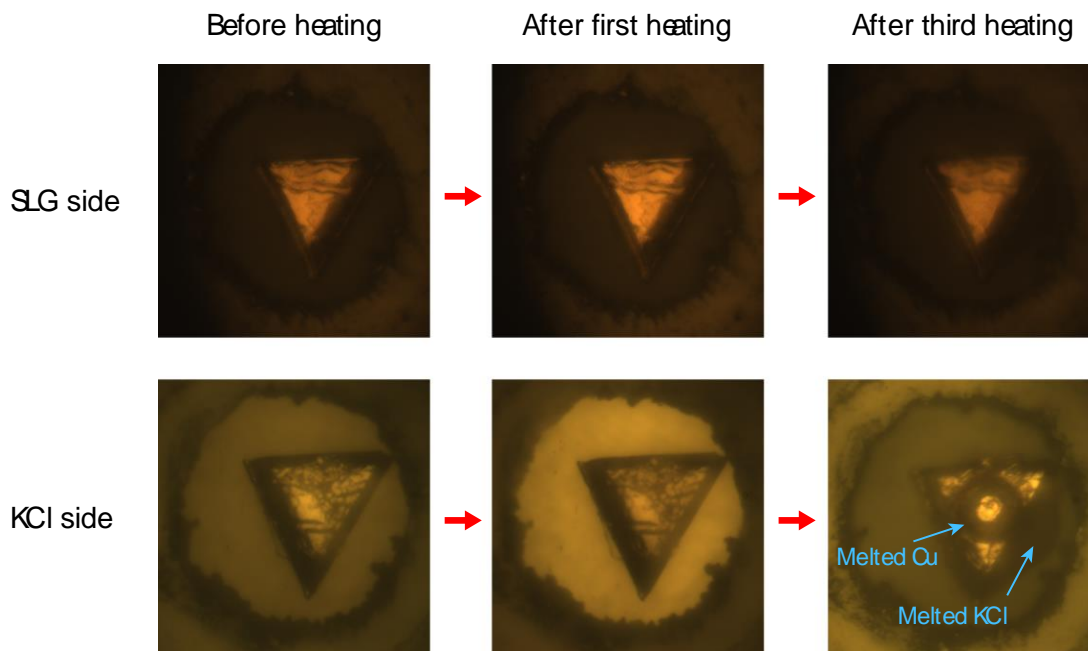


Figure 8-4 Microphotographs of the sample on the SLG side (top row) and KCl side (bottom row).

8.4 Residuals of hydrogenation

For Runs 1 and 2, SLG on Cu substrate are laser-heated at 8 and 20 GPa, respectively, in H₂ PTM and recovered at ambient pressure. Figure 8-6 (a) and (b) show the Raman spectra of Runs 1 and 2, respectively, by comparison between the pristine sample (prior loading) and recovered sample. D and D' peaks appear in the Raman spectra of the recovered samples of both Runs indicating that sp³- and/or vacancy-defects [12, 57] are created by the laser-heating. The result is in consistence with Smith *et al.* [78]. On the contrary, in control Run 3 which is He PTM experiment, $I(D)/I(G)$ ratios of the pristine and the recovered sample are not substantially different, while D' peak cannot be resolved. Therefore, the laser-heating of the SLG on Cu substrate in He PTM does not create additional defects in the sample unlike in H₂ PTM.

To justify that D peak presents either sp³-defect or vacancy-defect, $I(D)/I(D')$ is determined by fitting with Lorentzian lineshape of D peak and Breit-Wigner-Fano lineshape for D' peak [79, 80]. For the recovered sample in Run 1, $I(D)/I(D')$ of spots nearby the heated spot (S₁) are ~ 13, while $I(D)/I(D')$ of spots far from the heated spot (S₂) are ~ 7 (see Figure 8-7). The positions of S₁ and S₂ are marked in Figure 8-5. Thus, by Eckmann's condition, the defect occurs at S₁ is the sp³-defect, and at S₂ is the

vacancy-defect. However, the temperature of S_2 is lower than S_1 because of heat dissipation surround the heated spot. A creation of the vacancy-defect needs more energy of ion bombardment onto SLG than embedding adatoms revealed by a theoretical study using molecular dynamics simulation [81, 82]. Therefore, H_2 on the surface of S_2 cannot create the vacancy-defect, since its kinetic energy (from thermal energy) is lower than H_2 on the surface of S_1 . Thus, the D peaks at both S_1 and S_2 are emerged by the hydrogenation.

Figure 8-7 depicts the relation between $I(D)/I(G)$ and $I(D')/I(G)$ showing that N_D of the recovered samples in Run 1 and Run 2 are in Stage 1 and Stage 2 [59], respectively. For Stage 2, $I(D)/I(D')$ cannot be used to distinguish between sp^3 - and vacancy-defects. However, according to the discussion in the previous paragraph, the recovered sample in Run 2 should be hydrogenated SLG but has N_D higher than in Run 1. At 20 GPa, solid H_2 might cause shear stress on SLG creating edge-defect likewise solid Ar does. Even though the edge-defect contributes such small influence on $I(D)$, the majority of $I(D)$ of the recovered sample in Run 2 should be arisen by the hydrogenation.

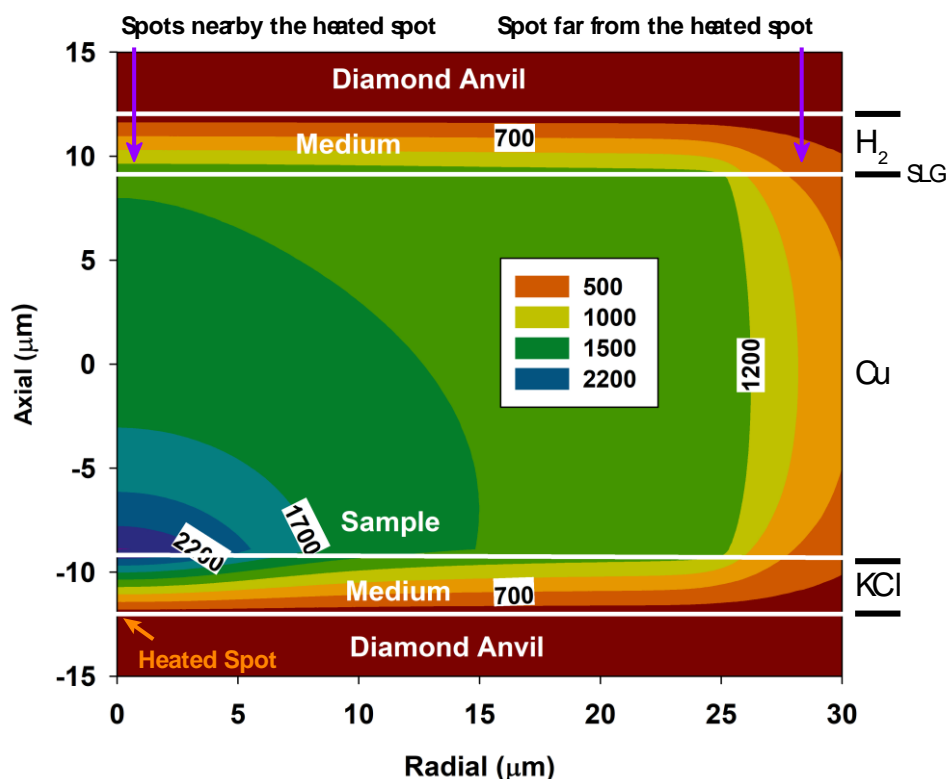


Figure 8-5 Contour plot of temperature gradient inside the *in situ* during laser heating.

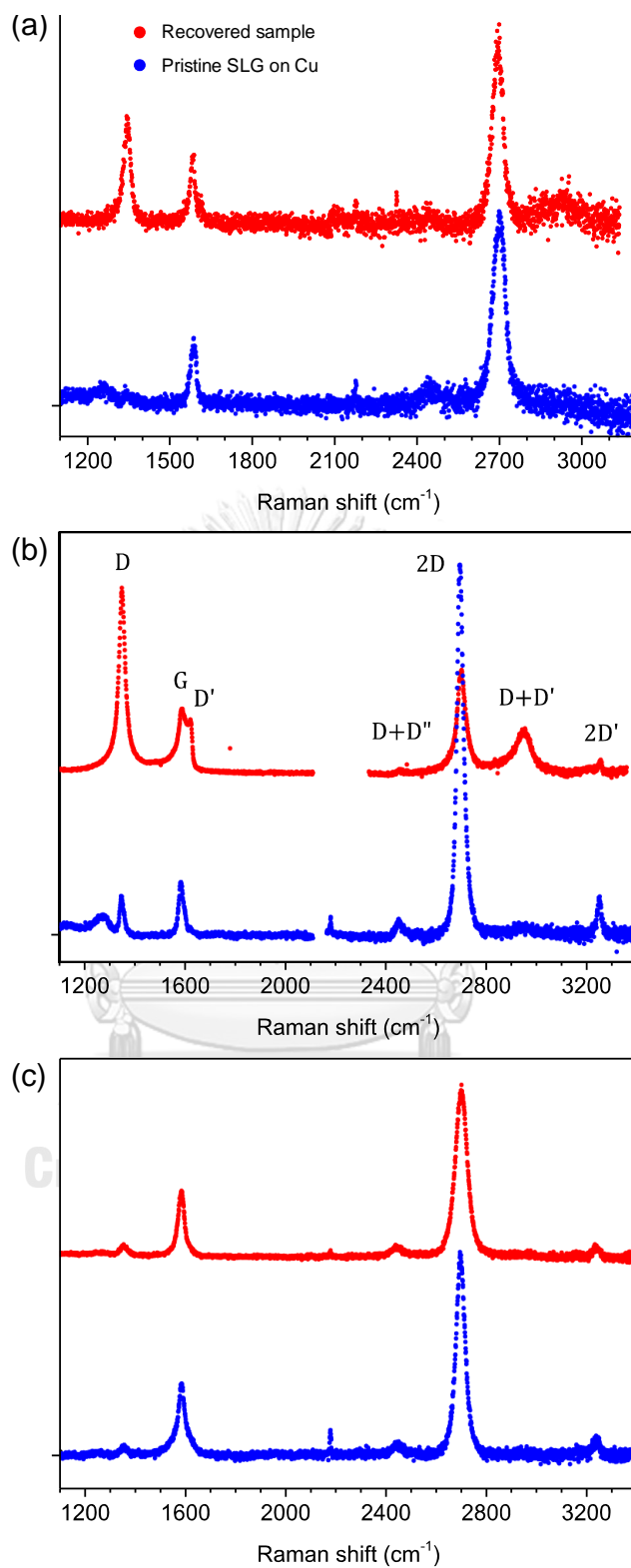


Figure 8-6 Raman spectra of the pristine SLG on Cu substrate (blue dots) and the recovered samples (red dots) of three Runs; (a) Run1, (b) Run2, and (c) Run3.

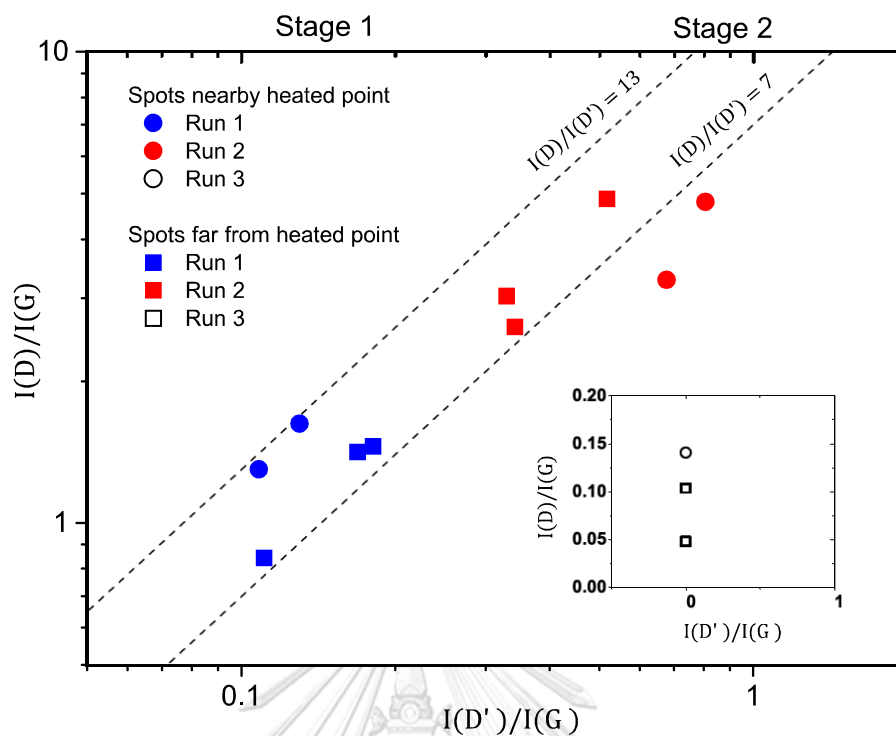


Figure 8-7 The intensity ratio plot between Raman peaks in the log-log scale is from the recovered samples of Run 1 (blue symbols), Run 2 (red symbols), and Run 3 (open symbols). The circle and square symbols are the spots nearby and far from the heated point, respectively (see Figure 8-5).

8.5 Pathway toward graphane at high pressure

The Raman spectra of the sample in Runs 1, 2 and 3 are collected using the 488 nm laser at 6, 1 and 3 different positions, respectively, around the sample repeatedly for each pressure point and after temperature treatment. By virtue of the 488 nm laser, the dispersion of 2D peak shifts its peak position emerging from the second-order peak of the diamond to be resolved in contrast to the conventional 532 nm laser. G and 2D peaks are fitted with Lorentzian lineshape to obtain the peak positions and linewidths. The Raman shifts of G and 2D peaks (ω_G and ω_{2D}) measured at various sample positions are averaged and plotted in Figure 8-9 as a function of pressure. The error bars are the standard deviation of the number of data points in that Run taken for each pressure point.

Figure 8-9 shows the evolution of the Raman spectra with pressure and after laser-heating in Runs 1 and 2. In compression, ω_G and ω_{2D} shift to higher frequencies as pressure increases (see Figure 8-9). In Run 2, G peak broadens at high pressure but remains clear to be resolved, in contrast with a 2D peak that broadens and coalesces with the background signal. In Run 1, ω_G and ω_{2D} shift to lower frequencies slightly after the first two laser-heating events but shift to lower frequencies noticeably after the third laser-heating, while the pressure changes about 1 GPa. It is worth noting that the

SLG side of the sample in Run 1 observed optically has no substantial change after it was laser-heated for three times as depicted in Figure 8-4. In decompression, ω_G and ω_{2D} shift to lower frequency unfollowing shifting paths in compression and forming hysteresis loops. The loops close near 3 GPa. Noting that the 2D peak in Run 1 cannot be resolved in some sample areas during decompression, in which case the data were averaged over less than 6 data points. The interpretation of the hysteresis loop will be discussed in the next section.

To show that the population of sp^3 -defects increases after the second laser heating in Run 2, N_D before and after laser heating are determined from $I(D)/I(G)$ using (4.12). This equation gives two solutions of N_D which result in Stage 1 and Stage 2 (see Table 8-1). We justify that before laser heating the defective SLG should be in Stage 1 which has $N_D = 0.90 \times 10^{12} \text{ cm}^{-2}$, while after the second laser heating the defective and/or hydrogenated SLG should be in Stage 2 which has N_D and/or hydrogen concentration $= 17.7 \times 10^{12} \text{ cm}^{-2}$ (see Table 8-1).

In the control Run 3 with He PTM to 9.4 GPa, there were slight drops of the Raman frequencies of the G and 2D peaks after heating (Figure 8-9). We find no substantial change in the intensity of these peaks. The pressure dependencies of the frequencies do show a small hysteresis loop similarly to the experiments with H_2 (see Figure 8-9).

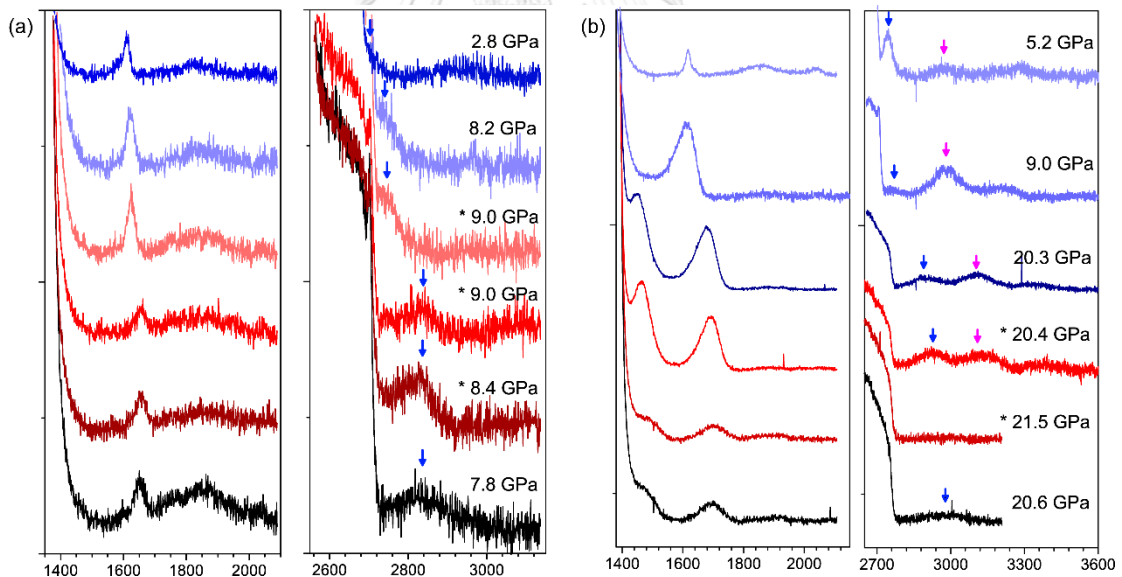


Figure 8-8 Raman spectra of (a) Run 1 and (b) Run 2 in compression (black line), after laser heating (reddish lines and labeled pressure value with the asterisk symbol), and in decompression (blueish lines). The blue arrow points the position of the 2D peak, and the pink arrow points the position of a new peak at various pressures.

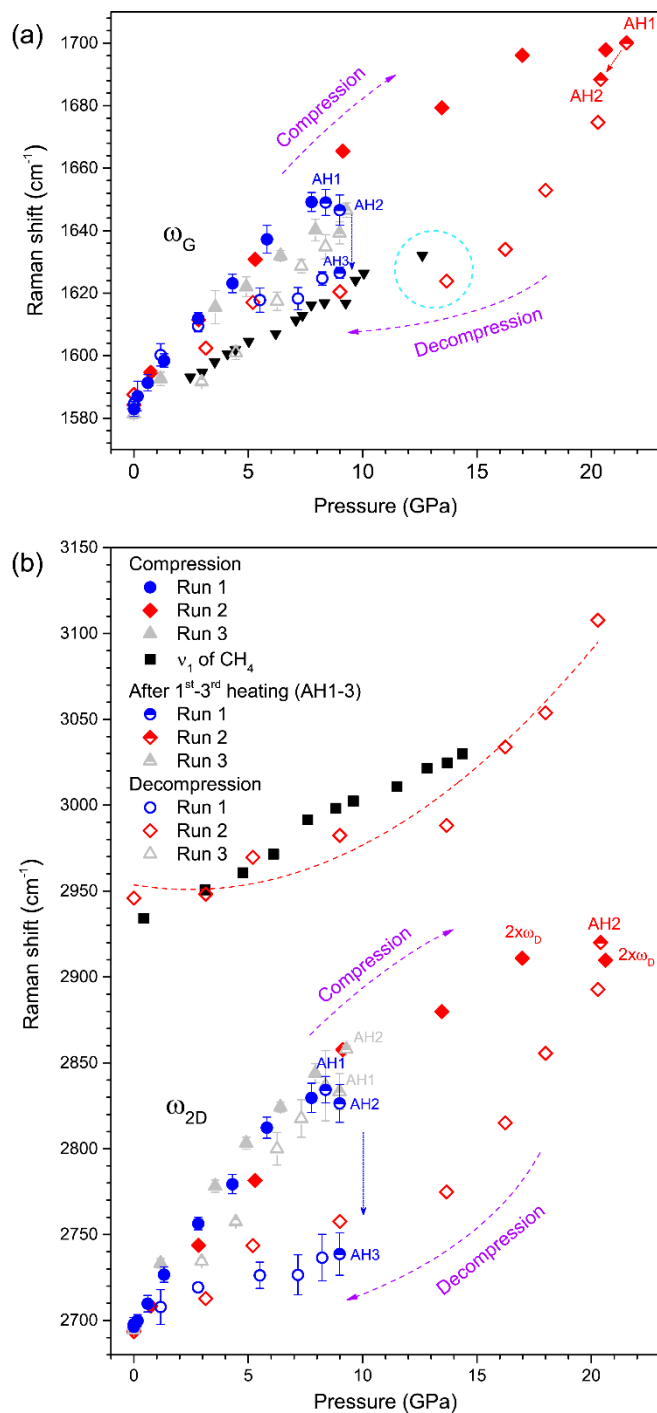


Figure 8-9 Raman shifts of peaks ω_G (a) and ω_{2D} (b) of SLG on Cu in Run 1 (blue circle), Run 2 (red diamond), and Run 3 (grey triangle) as a function of pressure during compression (filled symbols), after laser-heating (semi-filled symbols), and during decompression (open symbols). Red-dashed line in (b) is a guide to the eye of a new peak (see text) fitted with a quadratic equation. Dark down-triangles are the data for SLG on the diamond substrate from Ref. [21]. Black filled squares are the data for the ν_1 C-H stretching mode of methane obtained in this work in a separate experiment. The points labeled by $2\omega_D$ is the doubled frequency of the D peak (as the 2D peak could not be measured).

Table 8-1 The average distance between defect (L_D) and the defect concentration (N_D) are calculated using Equation (4.12). The parameters used in this calculation are $C_A = 3.84$ [12], $C_S = 0.87$, $r_A = 3.00$, $r_S = 1.00$ [57].

		P (GPa)	$\frac{I(D)}{I(G)}$	L_D (nm)		N_D ($\times 10^{12}$ cm $^{-2}$)	
				Stage 1	Stage 2	Stage 1	Stage 2
Run 2	Compression	20.6	1.93	5.95	1.62	0.90	12.1
	After first laser-heating	21.5	2.04	5.70	1.69	0.98	11.1
	After second laser-heating	20.4	1.48	7.19	1.34	0.62	17.7
	Decompression	20.3	1.35	7.64	1.26	0.55	20.1
	Recovered sample	0	4.4	N/A	N/A	N/A	N/A
Run 1	Recovered sample	0	3.27	3.10	3.10	3.33	3.33

The Raman spectra modifications after laser-heating are intriguing as they suggest a possible massive hydrogenation of SLG at high pressure in accord with the theoretical predictions [83]. Indeed, one would expect the G band to soften in graphene [84] due to a distortion of the graphene flat atomic sheets. Run 2 shows the most prominent observations, where we observed an increase in the intensity of all modes, which is consistent with the formation of sp^3 bonded carbon. Moreover, a new peak emerging in Run 2 at 3100 cm^{-1} appears after laser heating and remains on unloading down to ambient conditions that could signal the formation of the C-H bonding. Based on the frequency, this peak could be either D+D' or C-H stretching. This new peak could be either D+D' or C-H stretching modes which appear at a similar frequency at ambient pressure. Either interpretation can lead to the massive hydrogenation of SLG. For an illustration, the highly sp^3 -defected SLGs at ambient pressure also yield similar spectra where 2D and D+D' peaks broaden and merge, and $I(2D) / I(D + D') \approx 1$ (see Figure 4(b)) [60]. However, in view of the existence of the alternative explanations of the mentioned above phenomena, more definitive observations are needed to prove the massive hydrogenation.

8.6 Total stress and frictional stress on SLG

Figure 8-9 shows that ω_G and ω_{2D} shift to lower frequency drastically after laser-heating and their pressure dependencies reveal a hysteresis loop upon decompression. Similar phenomena have been noticed in previous works (albeit without laser-heating), where qualitatively, the more compressible substrate induces a compressive traction on the SLG, causing extra stress and hence an increase in ω_G and ω_{2D} [17, 21]. After laser-heating, SLG slips on the substrate, reducing these tractions, resulting in redshifted ω_G and ω_{2D} . This model provides a simple explanation to a variety of the pressure gradients observed for G band as well for its abrupt frequency drops under pressure.

Because ω_G is an intrinsic vibrational frequency of SLG subjugated to applied strain, the strain on SLG can be calculated without considering the substrate [17, 18],

$$\varepsilon(\omega_G) = -\beta(\omega_G - 1583) \quad (8.2)$$

where $\beta = 3.99 \times 10^{-4} \text{ cm}$ is a constant calculated from the Poisson's ratio, 0.167 [18], the Grüneisen parameter of phonon G mode, 1.90 (see Chapter 7 for details), and 1583 cm^{-1} which is ω_G for SLG on Cu substrate averaged from data in Run 1. Therefore, the highest strains of SLGs before laser-heating are 2.6% for Run 1 at 8 GPa, 4.6% for Run 2 at 20 GPa, and 2.3% for Run 3 at 8 GPa.

To account for the effect of the substrate on SLG we use a model, which accounts for friction between SLG and the Cu substrate. We assume that SLG is held by Cu substrate by a frictional stress ($\alpha_i \sigma_{Cu-SLG}$) causing an area of SLG to expand or shrink together with its substrate. Under pressure, SLG is affected by the external stress (σ_{ext}) and the frictional stress between SLG and Cu substrate (see a cartoon in Figure 1(c)). Thus, the total stress on SLG is

$$\sigma_{SLG} = \sigma_{ext} + \alpha_i \sigma_{Cu-SLG}, \quad (8.3)$$

where α_i is a coefficient of frictional stress between Cu surface and SLG at pressure point i and σ_{Cu-SLG} is a frictional stress supporting the equal deformation of the SLG area and Cu contact area (see Figure 7-1). The total stress, causing a compressive strain on SLG, shrinks the area of SLG per unit cell by,

$$-2\beta\Delta\omega_G + \beta^2(\Delta\omega_G)^2 = \lambda_{SLG}\sigma_{SLG}, \quad (8.4)$$

where the left-hand side is the area of SLG per unit cell written as a function of ω_G (see Chapter 7 for a derivation) and λ_{SLG} is a fitting parameter for SLG. Bousige *et al.* [21] shows that SLG on the diamond substrate has $\partial\omega_G/\partial P$ similar to graphite. Graphite is stacked of layers of graphene, where every layer is weakly connected to, so they contract independently under high pressure. Thus, the frictional stress between layers is assumed to be very small and can be neglected, yielding $\sigma_{SLG} \approx \sigma_{ext} = P$, and the Eq. 3 results as,

$$-2\beta\Delta\omega_G + \beta^2(\Delta\omega_G)^2 = \lambda_{SLG}P, \quad (8.5)$$

where P is pressure. Hence, we use Equation (4) to obtain λ_{SLG} by fitting $\Delta\omega_G$, which is data of SLG on the diamond substrate from Ref. [21], with P .

In the present work, the Raman frequencies ω_G and ω_{2D} as a function of σ_{SLG} are shown in Figure 8-10, where σ_{SLG} is calculated using Equation (3) where $\lambda_{SLG} = -0.0031 \text{ GPa}^{-1}$ (see Table 7-1). Figure 8-10 (a) shows that ω_G is linearized with σ_{SLG} , and the hysteresis loops for ω_{2D} (see Figure 8-10 (b)) are depleted in all runs except that of ω_{2D} in Run 1. Since the mechanical properties of partially hydrogenated SLG are similar to those of pristine SLG [85, 86], we assumed that the Grüneisen parameter of the phonon G mode and the Poisson's ratio of partially hydrogenated SLG are the same as those of the pristine SLG. Figure 8-10 suggests that the major origin of the hysteresis loop must come from the alteration of the frictional stress between Cu substrate and SLG.

The inset in Figure 8-10 (a) presents the coefficient of frictional stress, calculated by

$$\alpha_i = \frac{1}{\eta_i} \left[\frac{(\lambda_{Cu_1} - \eta_i \lambda_{SLG}) \sigma_{ext} + \lambda_{Cu_2} \sigma_{ext}^2}{(\lambda_{Cu_1} - \lambda_{SLG}) \sigma_{ext} + \lambda_{Cu_2} \sigma_{ext}^2} \right], \quad (8.6)$$

where λ_{Cu_1} and λ_{Cu_2} are fitting parameters of Cu area versus external stress extracted from Ref. [70] (see Chapter 7 for a derivation), and η_i is defined as

$$\left(\frac{V_{Cu}(P)}{V_{Cu}(0)} \right)^{2/3} - 1 = \eta_i (-2\beta \Delta\omega_G + \beta^2 (\Delta\omega_G)^2), \quad (8.7)$$

where $V_{Cu}(P)$ is a volume of Cu per unit cell as a function of pressure. After the third laser-heating in Run 1, α_i drops from 7.0 at 0.2 GPa to 2.2 at 2.8 GPa, and significantly drops to 0.4 (see the inset in Figure 8-10 (a)) indicating that SLG is almost detached from the Cu substrate completely. The similar results hold for Run 2 and Run 3 as well. Hence, laser-heating of the sample at a certain temperature loosens a contact between SLG and Cu substrate. The detachment may occur because the Cu lattice expands, but SLG lattice shrinks at high temperature [87-89].

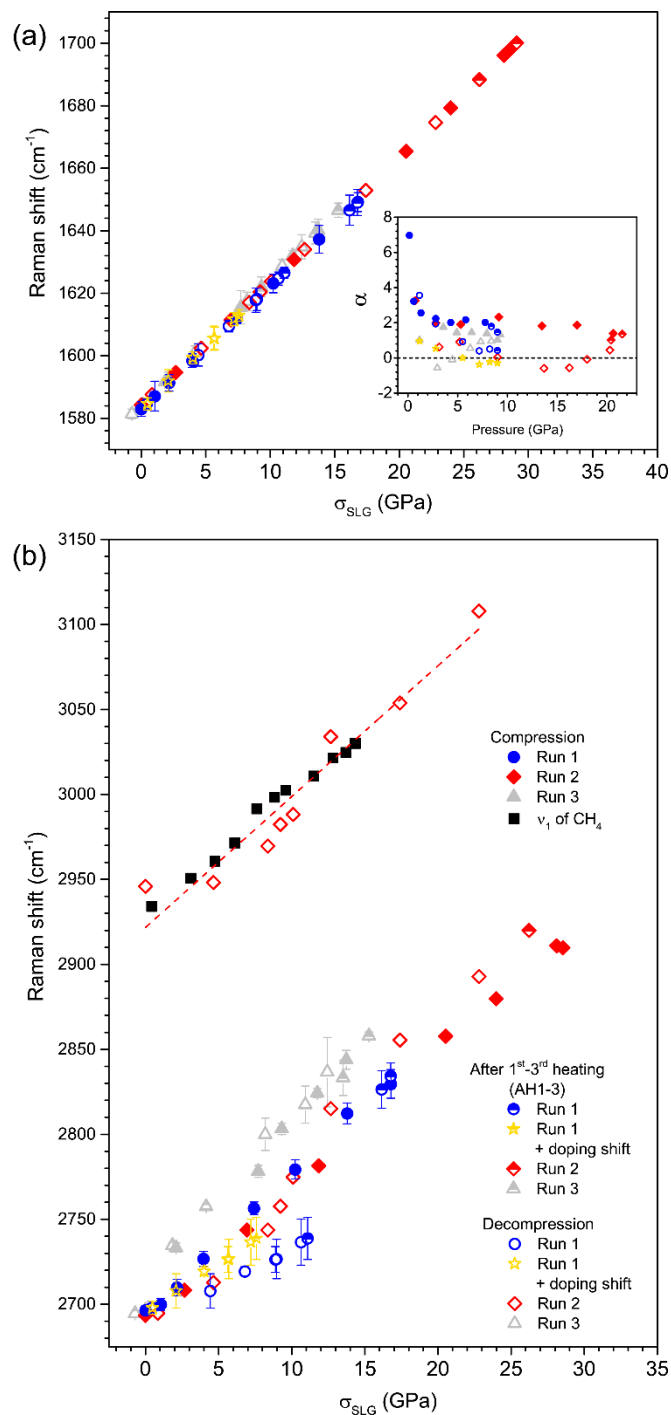


Figure 8-10 (a) ω_G and (b) ω_{2D} of SLG on Cu as a function of total in-plane stress acting on SLG. An inset in (a) shows the friction coefficient as a function of pressure deduced from our Raman frequency data. Red-dashed line in (b) is a guide to the eye of a new peak (see text) fitted with a linear equation. All symbols are the same representation as in Figure 5. Green stars are data corrected by $\Delta\omega_d$ (see text).

8.7 Correlation between ω_G and ω_{2D}

Here we discuss the correlation between ω_G and ω_{2D} , and why it changes after laser heating. On compression, ω_G is linearly related to ω_{2D} , and the $\partial\omega_{2D}/\partial\omega_G$ in Runs 1, 2 and 3 are 2.2, 2.0 and 2.5 (see Figure 8-11), respectively, which is in agreement with other experiments [17, 90, 91]. The dashed lines in Figure 8-11, extracted from Ref. [91], represent the correlation between ω_G and ω_{2D} of SLG when it is affected by purely strain (e_T line), purely hole-doped (e_H line), and concurrently strain and hole-doped [91]. In Run 1, the correlation between ω_G and ω_{2D} of the sample after third laser-heating shown in Figure 7 significantly changes from on the e_T line to near the e_H line. This indicates that the Raman spectrum of the quenched sample behaves as if it were hole-doped. Noting that Ref. [91] shows the line of hole-doping up to $15 \times 10^{12} \text{ cm}^{-2}$, we extrapolate the hole concentration lines up to $30 \times 10^{12} \text{ cm}^{-2}$ to cover our data by assuming that the line of hole concentration constantly changes with strain.

On the one hand, it may be unreliable to justify that the hydrogenated SLG is chemically hole-doped, since the $\partial\omega_{2D}/\partial\omega_G$ of strained SLG is not restricted to be 2.2 as we extracted from Ref. [91]. For example, the correlation between ω_G and ω_{2D} of Runs 2 and 3 are under and above, respectively, the e_T line (see Figure 8-11) in compression. On the other hand, to the best of our knowledge, there are no other explanations about the change of the correlation between ω_G and ω_{2D} of SLG. Therefore, we include the charge-doping effect, which shifts the ω_G as a function of charge concentration [92, 93], into the analysis. The Equation (8.2), hence, is reformulated to

$$\varepsilon(\omega_G, n) = -\beta(\omega_G - \Delta\omega_d(n, T) - 1583) \quad (8.8)$$

where $\Delta\omega_d(n, T)$ is added to correct a frequency shift as a function of charge-doping, n . The hole-doping concentration of each data point is extracted from the plot in Figure 8-11, and $\Delta\omega_d(n, T)$ can be calculated by [93]

$$\Delta\omega_d(n, T) = \frac{\alpha'}{\hbar} \text{P} \int_{-\infty}^{\infty} \frac{[f(\varepsilon - \varepsilon_F(n), T) - f(\varepsilon, T)] \varepsilon^2 \text{sgn}(\varepsilon)}{\varepsilon^2 - \frac{(\hbar\omega_0)^2}{4}} d\varepsilon \quad (8.9)$$

where $\alpha' = 4.39 \times 10^{-3}$, P is the principal part of the integral, f is the Fermi-Dirac distribution at $T = 300 \text{ K}$ and the Fermi level written as a function of n as [93]

$$\varepsilon_F(n) = \text{sgn}(n) \sqrt{n\pi} \hbar v_F \quad (8.10)$$

where v_F is the Fermi velocity and $\hbar v_F = 5.52 \text{ eV}\text{\AA}$. The recalculated strains on SLG using Equation (8.8) show that the hysteresis loop of ω_{2D} of Run 1 becomes smaller (see Figure 8-10 (b)). In the calculation, v_F is considered as an invariant parameter, but v_F should depend on applied strain [94], and charge-doping [95] that would be a reason for the persistent discrepancy between compression and decompression data of ω_{2D} of Run 1 (see Figure 8-10 (b)). However, to firmly support this conclusion more experiments need to be performed.

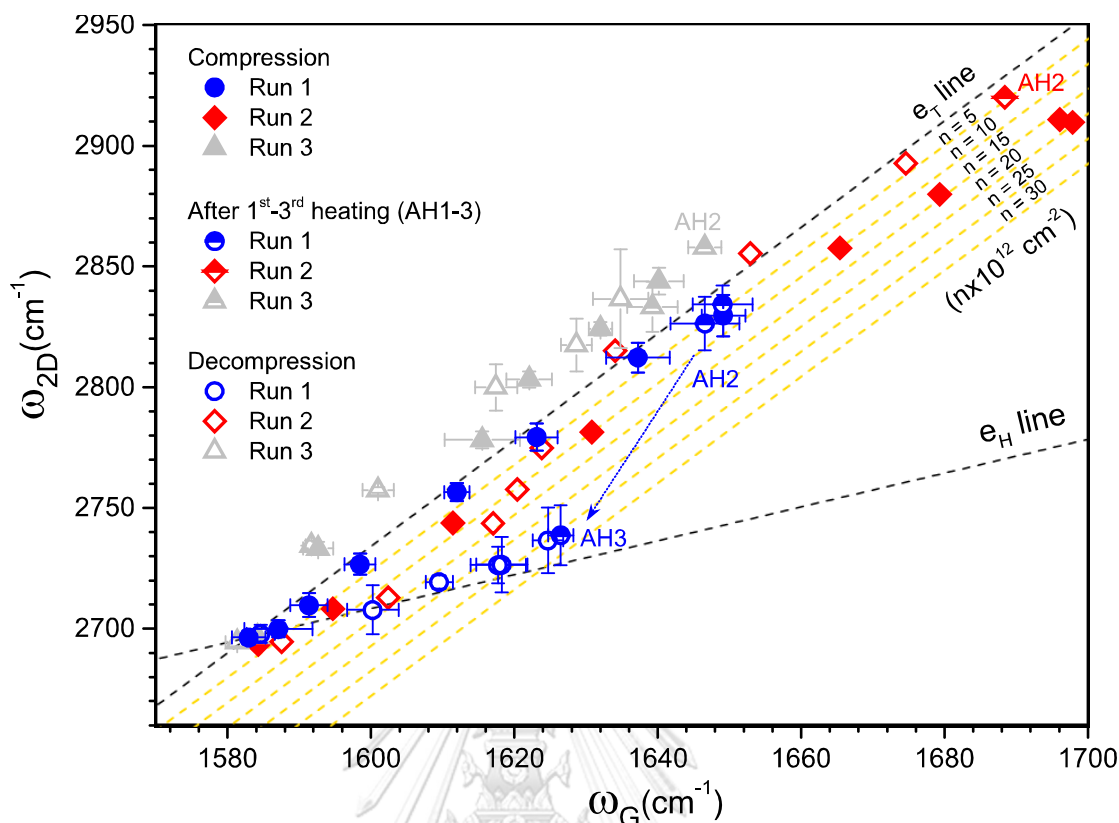


Figure 8-11 The correlation between ω_G and ω_{2D} of Run 1 (blue symbols), Run 2 (red symbols), and Run 3 (grey symbols).

8.8 Massive hydrogenation or detachment from the substrate?

We have discussed the possibilities of massive hydrogenation and the alteration of frictional stress between Cu substrate and SLG that cause the hysteresis loops of ω_G and ω_{2D} . The slipping model seems to explain the results well by diminishing of the hysteresis loops of ω_G and ω_{2D} shown in Figure 8-10. However, a downside of the slipping model is that we use all the parameters from the pristine SLG for hydrogenated SLG.

A theoretical study shows that the C-C bond length of graphane is longer than that of SLG, and the calculated optical phonon frequency at Γ -point of graphane is 1310 cm^{-1} at 0 GPa and 1350 cm^{-1} at 10 GPa [84], indicating the cause of the softening of ω_G of SLG after laser heating. Even though graphane is not thermodynamically stable at ambient pressure [83], it becomes stable under pressure and it could be metastable down to almost ambient pressure as evidenced by the presence of 3100 cm^{-1} band on unloading in Run 2 (see Figure 8-8 (b)), which can be interpreted as the C-H stretching mode. The theoretical study using Monte Carlo simulation demonstrated that H atoms prefer to form dangling bonds with C atoms on both sides of SLG and stay in close proximity to each other [96]. H_2 could penetrate through the gap between Cu and SLG to hydrogenate SLG from the substrate side during laser heating, causing a massive

hydrogenation to occur. For example, a dashed circle in Figure 8-9 (a) marks that ω_G of hydrogenated SLG on Cu substrate is lower than ω_G of SLG on diamond substrate at similar pressure. For this case, the massive hydrogenation, causing the average C-C bond length of hydrogenated SLG longer than SLG, is a better explanation. Therefore, the massive hydrogenation and the detachment together can cause a tremendous redshift of ω_G .

Moreover, in decompression, ω_G of hydrogenated SLG on Cu substrate is higher than ω_G of SLG on the diamond substrate at ~ 5 GPa (see open trapezoid and down-triangle symbols at 5 GPa in Figure 8-9 (a)). The shortening of C-C bond length as pressure decreases can be explained by dehydrogenation from massively to partially hydrogenated SLG.

Yet another alternative explanation of the drop-in ω_G after laser-heating could be a structural transition in SLG similar to that reported in graphite [97, 98] or graphdiyne [99]. Evidently, the linewidth of the G band at 4.6% of compressive strain is six-fold larger than that of pristine SLG (see Figure 8-12), similar to phase transformation in graphite [100, 101]. The broadened G peak may come from the convolution of several peaks appearing because of the existence of several C-C bond lengths in the structure as well as a large disorder or even amorphization [102] originating from the corrugation of SLG on Cu substrate. However, to discuss this phenomenon qualitatively, more data is needed which is beyond the scope of the present work.

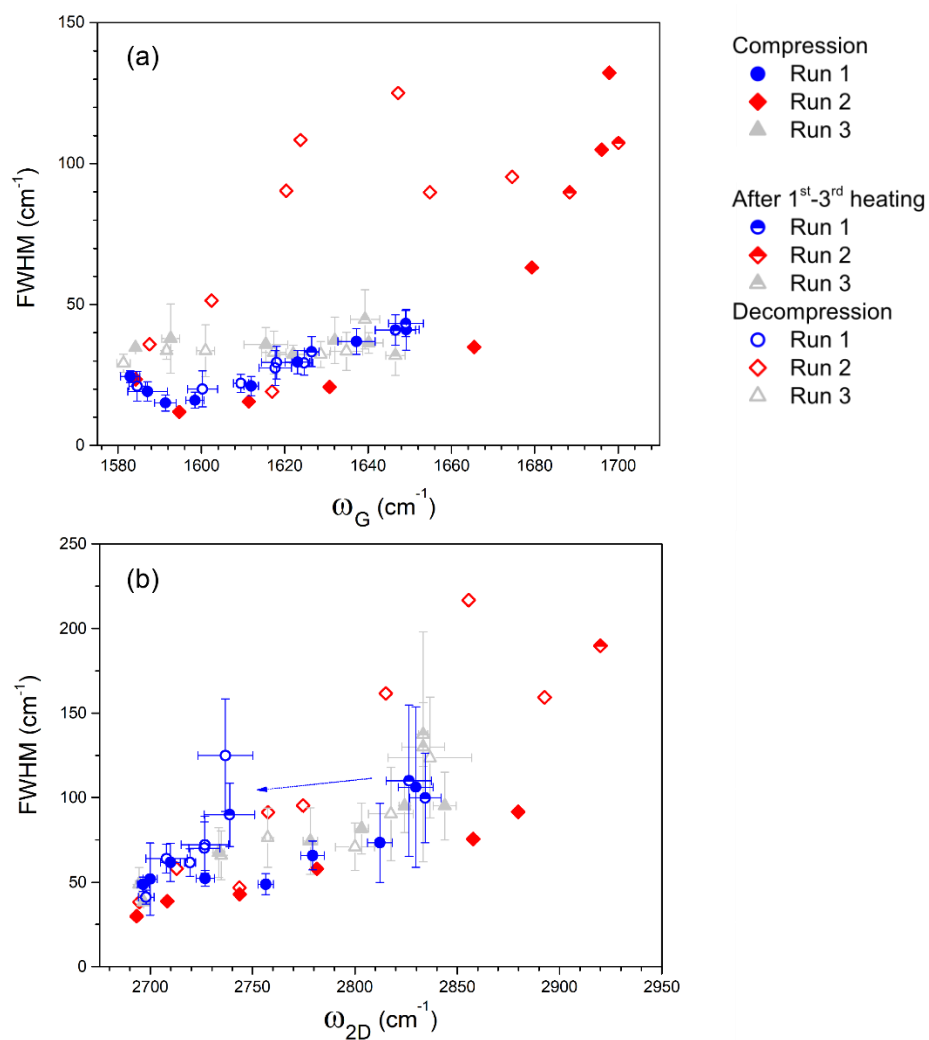


Figure 8-12 (a) The relation between FWHM(G) and ω_G , and (b) the relation between FWHM(2D) and ω_{2D} .

9 Conclusion

We perform a series of studies on hydrogenated graphene in theoretical and experimental aspects. We start with BLG where it is fully passivated by H atoms and C atoms between two layers will form sp^3 -bonding in which a product is hydrogenated diamondized BLG. We show that the C atoms that form sp^3 -bonding will decompose back to be BLG if there are no H atoms cooperating. Two types of hydrogenated diamondized BLG formed from AB- and AA-stacked BLG are H-diamondene and H-lonsdaleitene, respectively (see Figure 5-2). The convex hull in Figure 5-5 presents the phase stability of both phases which are destabilized by the phonon energy. Even though they are dynamically stable up to 1000 K confirmed by AIMD simulation. We also suggest the Raman and IR frequencies that could appear in the experiment if H-diamondene and H-lonsdaleitene can be synthesized successfully. The Raman and IR active modes of both diamondized hydrogenated BLGs are approximate at ~ 400 , ~ 700 , ~ 1100 , ~ 1300 and $\sim 2900 \text{ cm}^{-1}$ (see Table 5-2 and Table 5-3 for exact values). Their frequencies contrast to the vibrational mode of BLG because of the changes in bond length and degree of freedom. For hydrogenated SLG, graphane is most energetically favorable even at 300 K in contrast to diamondized hydrogenated BLG. The compressive strain can help the partially hydrogenated SLG to be energetically favorable instead of graphane, however, it needs at least 10% compressive strain to be stable which is difficult to achieve in the experiment.

We attempt to synthesis highly hydrogenated SLG using laser-heating at high pressure. The Raman spectroscopy with the 488 nm laser is employed to study the alteration of the chemical reaction between SLG and solid H_2 at 8 and 20 GPa. SLG on Cu substrate is at 2.2% and 4.6% compressive strain before it was laser-heating at 8 and 20 GPa, respectively. The results of the recovered samples demonstrate that the degree of hydrogenation is greater when the chemical reaction occurs at higher pressure (see Figure 8-6). Moreover, by using a mathematical model, we show that the SLG film slippers from Cu substrate caused by the thermal treatment which is a root of hysteresis loops of ω_G and ω_{2D} (see Figure 8-9 and Figure 8-10). Hydrogenated SLG also behaves likely being hole-doped as derived from the correlation between ω_G and ω_{2D} (see Figure 8-11). However, further study is a must to firmly support this phenomenon.

Appendix A: List of Abbreviations

2d	2-dimensional
AIMD	<i>Ab-initio</i> Molecular Dynamics
BLG	Bilayer Graphene
CBM	Conduction Band Minimum
DAC	Diamond Anvil Cell
DFT	Density Functional Theory
DOS	Density of States
FWHM	Full Width at Half Maximum
GGA	Generalized Gradient Approximation
IR	Infrared
KS	Kohn-Sham
LDA	Local Density Approximation
PAW	Projector Augmented Wave
PBE	Perdew-Burke-Ernzerhof
PTM	Pressure Transmitting Medium
SCF	Self-consistence Field
SLG	Single-layer Graphene
STM	Scanning Tunneling Microscope
UV	Ultraviolet
VBM	Valence Band Maximum
XC	Exchange-correlation

REFERENCES

1. Novoselov, K.S., et al., *Two-dimensional gas of massless Dirac fermions in graphene*. Nature, 2005. **438**(7065): p. 197-200.
2. Bostwick, A., et al., *Quasiparticle dynamics in graphene*. Nature Physics, 2007. **3**(1): p. 36-40.
3. Ishigami, M., et al., *Atomic structure of graphene on SiO₂*. Nano Letters, 2007. **7**(6): p. 1643-1648.
4. Katsnelson, M.I. and A.K. Geim, *Electron scattering on microscopic corrugations in graphene*. Philosophical Transactions of the Royal Society a-Mathematical Physical and Engineering Sciences, 2008. **366**(1863): p. 195-204.
5. Fasolino, A., J.H. Los, and M.I. Katsnelson, *Intrinsic ripples in graphene*. Nature Materials, 2007. **6**(11): p. 858-861.
6. Fan, X.Y., R. Nouchi, and K. Tanigaki, *Effect of Charge Puddles and Ripples on the Chemical Reactivity of Single Layer Graphene Supported by SiO₂/Si Substrate*. Journal of Physical Chemistry C, 2011. **115**(26): p. 12960-12964.
7. Thomsen, J.D., et al., *Suppression of intrinsic roughness in encapsulated graphene*. Physical Review B, 2017. **96**(1).
8. Dean, C.R., et al., *Boron nitride substrates for high-quality graphene electronics*. Nature Nanotechnology, 2010. **5**(10): p. 722-726.
9. Ferrari, A.C. and D.M. Basko, *Raman spectroscopy as a versatile tool for studying the properties of graphene*. Nature Nanotechnology, 2013. **8**(4): p. 235-246.
10. Malard, L.M., et al., *Raman spectroscopy in graphene*. Physics Reports-Review Section of Physics Letters, 2009. **473**(5-6): p. 51-87.
11. Malard, L.M., et al., *Group-theory analysis of electrons and phonons in N-layer graphene systems*. Physical Review B, 2009. **79**(12).
12. Cancado, L.G., et al., *Quantifying Defects in Graphene via Raman Spectroscopy at Different Excitation Energies*. Nano Letters, 2011. **11**(8): p. 3190-3196.
13. Yuk, J.M., et al., *Superstructural defects and superlattice domains in stacked graphene*. Carbon, 2014. **80**: p. 755-761.
14. Kirilenko, D.A. and P.N. Brunkov, *Measuring the height-to-height correlation function of corrugation in suspended graphene*. Ultramicroscopy, 2016. **165**: p. 1-7.
15. Kirilenko, D.A., A.T. Dideykin, and G. Van Tendeloo, *Measuring the corrugation amplitude of suspended and supported graphene*. Physical Review B, 2011. **84**(23).
16. Marianetti, C.A. and H.G. Yevick, *Failure Mechanisms of Graphene under Tension*. Physical Review Letters, 2010. **105**(24).

17. Mohiuddin, T.M.G., et al., *Uniaxial strain in graphene by Raman spectroscopy: G peak splitting, Gruneisen parameters, and sample orientation*. Physical Review B, 2009. **79**(20).
18. Cheng, Y.C., et al., *Gruneisen parameter of the G mode of strained monolayer graphene*. Physical Review B, 2011. **83**(11).
19. Yoon, D., Y.W. Son, and H. Cheong, *Strain-Dependent Splitting of the Double-Resonance Raman Scattering Band in Graphene*. Physical Review Letters, 2011. **106**(15).
20. Proctor, J.E., et al., *High-pressure Raman spectroscopy of graphene*. Physical Review B, 2009. **80**(7).
21. Bousige, C., et al., *Biaxial Strain Transfer in Supported Graphene*. Nano Letters, 2017. **17**(1): p. 21-27.
22. Nicolle, J., et al., *Pressure-Mediated Doping in Graphene*. Nano Letters, 2011. **11**(9): p. 3564-3568.
23. Filintoglou, K., et al., *Raman spectroscopy of graphene at high pressure: Effects of the substrate and the pressure transmitting media*. Physical Review B, 2013. **88**(4).
24. Kyhl, L., et al., *Exciting H-2 Molecules for Graphene Functionalization*. Acs Nano, 2018. **12**(1): p. 513-520.
25. Balog, R., et al., *Controlling Hydrogenation of Graphene on Ir(111)*. Acs Nano, 2013. **7**(5): p. 3823-3832.
26. Balog, R., et al., *Bandgap opening in graphene induced by patterned hydrogen adsorption*. Nature Materials, 2010. **9**(4): p. 315-319.
27. Jorgensen, J.H., et al., *Symmetry-Driven Band Gap Engineering in Hydrogen Functionalized Graphene*. Acs Nano, 2016. **10**(12): p. 10798-10807.
28. Son, J., et al., *Hydrogenated monolayer graphene with reversible and tunable wide band gap and its field-effect transistor*. Nature Communications, 2016. **7**.
29. Haberer, D., et al., *Tunable Band Gap in Hydrogenated Quasi-Free-standing Graphene*. Nano Letters, 2010. **10**(9): p. 3360-3366.
30. Elias, D.C., et al., *Control of Graphene's Properties by Reversible Hydrogenation: Evidence for Graphane*. Science, 2009. **323**(5914): p. 610-613.
31. Kyhl, L., et al., *Hydrogenated graphene on Ir(111): A high-resolution electron energy loss spectroscopy study of the vibrational spectrum*. Physical Review B, 2016. **93**(11).
32. Sofo, J.O., A.S. Chaudhari, and G.D. Barber, *Graphane: A two-dimensional hydrocarbon*. Physical Review B, 2007. **75**(15).
33. Levy, N., et al., *Strain-Induced Pseudo-Magnetic Fields Greater Than 300 Tesla in Graphene Nanobubbles*. Science, 2010. **329**(5991): p. 544-547.

34. Leconte, N., et al., *Magnetism-Dependent Transport Phenomena in Hydrogenated Graphene: From Spin-Splitting to Localization Effects*. *ACS Nano*, 2011. **5**(5): p. 3987-3992.
35. Soriano, D., et al., *Spin transport in hydrogenated graphene*. *2d Materials*, 2015. **2**(2).
36. Gonzalez-Herrero, H., et al., *Atomic-scale control of graphene magnetism by using hydrogen atoms*. *Science*, 2016. **352**(6284): p. 437-441.
37. Kim, H., J. Bang, and J. Kang, *Robust ferromagnetism in hydrogenated graphene mediated by spin-polarized pseudospin*. *Scientific Reports*, 2018. **8**.
38. Tucek, J., et al., *Room temperature organic magnets derived from sp(3) functionalized graphene*. *Nature Communications*, 2017. **8**.
39. Palacios, J.J., J. Fernandez-Rossier, and L. Brey, *Vacancy-induced magnetism in graphene and graphene ribbons*. *Physical Review B*, 2008. **77**(19).
40. Yazyev, O.V. and L. Helm, *Defect-induced magnetism in graphene*. *Physical Review B*, 2007. **75**(12).
41. Zhang, Y., et al., *Scanning Tunneling Microscopy of the pi Magnetism of a Single Carbon Vacancy in Graphene*. *Physical Review Letters*, 2016. **117**(16).
42. Ulman, K. and S. Narasimhan, *Point defects in twisted bilayer graphene: A density functional theory study*. *Physical Review B*, 2014. **89**(24).
43. Zapata-Pena, R., B.S. Mendoza, and A.I. Shkrebtii, *Pure spin current injection in hydrogenated graphene structures*. *Physical Review B*, 2017. **96**(19).
44. Lee, C., et al., *Measurement of the elastic properties and intrinsic strength of monolayer graphene*. *Science*, 2008. **321**(5887): p. 385-388.
45. Gao, Y., et al., *Ultrahard carbon film from epitaxial two-layer graphene*. *Nature Nanotechnology*, 2018. **13**(2): p. 133-+.
46. Kvashnin, A.G. and P.B. Sorokin, *Lonsdaleite Films with Nanometer Thickness*. *Journal of Physical Chemistry Letters*, 2014. **5**(3): p. 541-548.
47. Barboza, A.P.M., et al., *Room-Temperature Compression-Induced Diamondization of Few-Layer Graphene*. *Advanced Materials*, 2011. **23**(27): p. 3014-+.
48. Pakornchote, T., et al., *Phase stabilities and vibrational analysis of hydrogenated diamondized bilayer graphenes: A first principles investigation*. *Carbon*, 2019. **146**: p. 468-475.
49. Martins, L.G.P., et al., *Raman evidence for pressure-induced formation of diamondene*. *Nature Communications*, 2017. **8**.
50. Piazza, F., et al., *Low temperature, pressureless sp(2) to sp(3) transformation of ultrathin, crystalline carbon films*. *Carbon*, 2019. **145**: p. 10-22.
51. Hohenberg, P. and W. Kohn, *Inhomogeneous Electron Gas*. *Physical Review B*, 1964. **136**(3b): p. B864-+.

52. Kohn, W. and L.J. Sham, *Self-Consistent Equations Including Exchange and Correlation Effects*. Physical Review, 1965. **140**(4a): p. 1133-&.
53. Griffiths, R.B., *Consistent quantum theory*. 2002, Cambridge ; New York: Cambridge University Press. xvi, 391 p.
54. Blochl, P.E., *The projector augmented wave (PAW) method: Basics and applications*. Abstracts of Papers of the American Chemical Society, 1999. **217**: p. U690-U690.
55. Kresse, G. and D. Joubert, *From ultrasoft pseudopotentials to the projector augmented-wave method*. Physical Review B, 1999. **59**(3): p. 1758-1775.
56. Venezuela, P., M. Lazzeri, and F. Mauri, *Theory of double-resonant Raman spectra in graphene: Intensity and line shape of defect-induced and two-phonon bands*. Physical Review B, 2011. **84**(3).
57. Lucchese, M.M., et al., *Quantifying ion-induced defects and Raman relaxation length in graphene*. Carbon, 2010. **48**(5): p. 1592-1597.
58. Ferrari, A.C. and J. Robertson, *Interpretation of Raman spectra of disordered and amorphous carbon*. Physical Review B, 2000. **61**(20): p. 14095-14107.
59. Eckmann, A., et al., *Probing the Nature of Defects in Graphene by Raman Spectroscopy*. Nano Letters, 2012. **12**(8): p. 3925-3930.
60. Eckmann, A., et al., *Raman study on defective graphene: Effect of the excitation energy, type, and amount of defects*. Physical Review B, 2013. **88**(3).
61. Casiraghi, C., et al., *Raman Spectroscopy of Graphene Edges*. Nano Letters, 2009. **9**(4): p. 1433-1441.
62. Gupta, A.K., et al., *Probing Graphene Edges via Raman Scattering*. Acs Nano, 2009. **3**(1): p. 45-52.
63. You, Y.M., et al., *Edge chirality determination of graphene by Raman spectroscopy*. Applied Physics Letters, 2008. **93**(16).
64. Fateley, W.G., *Infrared and Raman selection rules for molecular and lattice vibrations: the correlation method*. 1972, New York,: Wiley-Interscience. vii, 222 p.
65. Ferraro, J.R., K. Nakamoto, and C.W. Brown, *Introductory Raman spectroscopy*. 2nd ed. 2003, Amsterdam ; Boston: Academic Press. xiii, 434 p.
66. Mykolajewycz, R., A. Smakula, and J. Kalnajs, *High-Precision Density Determination of Natural Diamonds*. Journal of Applied Physics, 1964. **35**(6): p. 1773-&.
67. Wang, S.Q. and H.Q. Ye, *Ab initio elastic constants for the lonsdaleite phases of C, Si and Ge*. Journal of Physics-Condensed Matter, 2003. **15**(30): p. 5307-5314.
68. Tan, P.H., et al., *The shear mode of multilayer graphene*. Nature Materials, 2012. **11**(4): p. 294-300.

69. Tong, X., et al., *Phonons in Si-24 at simultaneously elevated temperature and pressure*. Physical Review B, 2017. **95**(9).
70. Liu, L.G., et al., *Comparative Compressibility of Cu, Ag and Au*. Journal of Physics and Chemistry of Solids, 1990. **51**(5): p. 435-438.
71. Pakornchote, T., et al., *Raman spectroscopy on hydrogenated graphene under high pressure*. Carbon, 2020. **156**: p. 549-557.
72. Goncharov, A.F., *Raman Spectroscopy at High Pressures*. International Journal of Spectroscopy, 2012. **2012**.
73. Mao, H.K., J. Xu, and P.M. Bell, *Calibration of the Ruby Pressure Gauge to 800-Kbar under Quasi-Hydrostatic Conditions*. Journal of Geophysical Research-Solid Earth and Planets, 1986. **91**(B5): p. 4673-4676.
74. Dewaele, A., et al., *Compression curves of transition metals in the Mbar range: Experiments and projector augmented-wave calculations*. Physical Review B, 2008. **78**(10).
75. Japel, S., et al., *Melting of copper and nickel at high pressure: The role of d electrons*. Physical Review Letters, 2005. **95**(16).
76. Boehler, R., M. Ross, and D.B. Boercker, *High-pressure melting curves of alkali halides*. Physical Review B, 1996. **53**(2): p. 556-563.
77. Montoya, J.A. and A.F. Goncharov, *Finite element calculations of the time dependent thermal fluxes in the laser-heated diamond anvil cell*. Journal of Applied Physics, 2012. **111**(11).
78. Smith, D., et al., *Hydrogenation of Graphene by Reaction at High Pressure and High Temperature*. Acs Nano, 2015. **9**(8): p. 8279-8283.
79. Hasdeo, E.H., et al., *Breit-Wigner-Fano line shapes in Raman spectra of graphene*. Physical Review B, 2014. **90**(24).
80. Demtroeder, W., *Laser spectroscopy I : basic principles*. 5th edition. ed. 2014, New York: Springer. pages cm.
81. Qin, X.M., et al., *Molecular dynamics simulation of graphene bombardment with Si ion*. Journal of Molecular Structure, 2014. **1061**: p. 19-25.
82. Wu, X., et al., *Molecular dynamics simulation of graphene sheets joining under ion beam irradiation*. Carbon, 2014. **66**: p. 31-38.
83. Naumoya, A.S., S.V. Lepeshkin, and A.R. Oganov, *Hydrocarbons under Pressure: Phase Diagrams and Surprising New Compounds in the C-H System*. Journal of Physical Chemistry C, 2019. **123**(33): p. 20497-20501.
84. Wen, X.D., et al., *Graphane sheets and crystals under pressure*. Proceedings of the National Academy of Sciences of the United States of America, 2011. **108**(17): p. 6833-6837.
85. Cadelano, E., et al., *Elastic properties of hydrogenated graphene*. Physical Review B, 2010. **82**(23).

86. Weerasinghe, A., et al., *Mechanical properties of hydrogenated electron-irradiated graphene*. Journal of Applied Physics, 2016. **120**(12).
87. Bao, W.Z., et al., *Controlled ripple texturing of suspended graphene and ultrathin graphite membranes*. Nature Nanotechnology, 2009. **4**(9): p. 562-566.
88. Mounet, N. and N. Marzari, *First-principles determination of the structural, vibrational and thermodynamic properties of diamond, graphite, and derivatives*. Physical Review B, 2005. **71**(20).
89. Yoon, D., Y.W. Son, and H. Cheong, *Negative Thermal Expansion Coefficient of Graphene Measured by Raman Spectroscopy*. Nano Letters, 2011. **11**(8): p. 3227-3231.
90. Zabel, J., et al., *Raman Spectroscopy of Graphene and Bilayer under Biaxial Strain: Bubbles and Balloons*. Nano Letters, 2012. **12**(2): p. 617-621.
91. Lee, J.E., et al., *Optical separation of mechanical strain from charge doping in graphene*. Nature Communications, 2012. **3**.
92. Lazzeri, M., A.M. Saitta, and F. Mauri, *Breakdown of the adiabatic approximation in a doped graphene monolayer and in metallic carbon nanotubes*. Physica Status Solidi B-Basic Solid State Physics, 2007. **244**(11): p. 4118-4123.
93. Pisana, S., et al., *Breakdown of the adiabatic Born-Oppenheimer approximation in graphene*. Nature Materials, 2007. **6**(3): p. 198-201.
94. Pereira, V.M., A.H. Castro Neto, and N.M.R. Peres, *Tight-binding approach to uniaxial strain in graphene*. Physical Review B, 2009. **80**(4).
95. Elias, D.C., et al., *Dirac cones reshaped by interaction effects in suspended graphene*. Nature Physics, 2011. **7**(9): p. 701-704.
96. Xiang, H.J., et al., *"Narrow" Graphene Nanoribbons Made Easier by Partial Hydrogenation*. Nano Letters, 2009. **9**(12): p. 4025-4030.
97. Goncharov, A.F., *Graphite at high pressures: Amorphization at 44 GPa*. High Pressure Research, 1992. **8**(4): p. 607-616.
98. Goncharov, A.F., I.N. Makarenko, and S.M. Stishov, *Graphite at pressures up to 55 GPa: Optical properties and raman spectra*. High Pressure Research, 1990. **4**(1-6): p. 345-347.
99. Wang, Y., et al., *Graphdiyne under pressure: A Raman study*. Applied Physics Letters, 2018. **113**(2).
100. Amsler, M., et al., *Crystal Structure of Cold Compressed Graphite*. Physical Review Letters, 2012. **108**(6).
101. Hanfland, M., H. Beister, and K. Syassen, *Graphite under pressure: Equation of state and first-order Raman modes*. Physical Review B, 1989. **39**(17): p. 12598-12603.
102. Schwan, J., et al., *Raman spectroscopy on amorphous carbon films*. Journal of Applied Physics, 1996. **80**(1): p. 440-447.



จุฬาลงกรณ์มหาวิทยาลัย
CHULALONGKORN UNIVERSITY



จุฬาลงกรณ์มหาวิทยาลัย
CHULALONGKORN UNIVERSITY

VITA

NAME	Teerachote Pakornchote
DATE OF BIRTH	06 Sept 1988
PLACE OF BIRTH	Bangkok, Thailand
INSTITUTIONS ATTENDED	Bachelor of Science from Department of Physics, Faculty of Science, Chulalongkorn University, Thailand Master of Science from Department of Physics, Faculty of Science, Chulalongkorn University, Thailand
PUBLICATION	<ol style="list-style-type: none">1. Pakornchote T, Pinsook U and Bovornratanaraks T, Structural phase transition of scandium trihydride under high pressure by using ab initio, Siam Physics Congress SPC2013, page 313-16 (2013).2. Pakornchote T, Pinsook U and Bovornratanaraks T, The hcp to fcc transformation path of scandium trihydride under high pressure, J. Phys. Condens. Matter 26, 025405 (2014).3. Pakornchote T, Bovornratanaraks T, Vannarat S and Pinsook U, Strong influence to properties of ScH₃ hcp phase by off-site symmetry positions of hydrogen atoms, Solid State Commun. 225, 48-55 (2016).4. Tunghathaithip N, Pakornchote T, Phaisangittisakul N, Bovornratanaraks T and Pinsook U, Pressure effect on hydrogen atoms near metal plane in hcp phase of rare-earth metal trihydrides, Solid State Commun. 231-232, 48-52 (2016).5. Klinkla R, Sakulsupich V, Pakornchote T, Pinsook U and Bovornratanaraks T, The crucial role of density functional nonlocality and on-axis CH₃NH₃ rotation induced I₂ formation in hybrid organic-inorganic CH₃NH₃PbI₃ cubic perovskite, Sci. Rep. 8, 13161 (2018).6. Pakornchote T, Ektarawong A, Alling B, Pinsook U, Tancharakorn S, Busayaporn W and Bovornratanaraks T, Phase stabilities and vibrational analysis of hydrogenated diamondized bilayer graphenes: A first principles investigation, Carbon 146, 468-75 (2019).7. Wang Y, Zhang X, Jiang SQ, Geballe ZM, Pakornchote T, Somayazulu M, Prakapenka VB, Greenberg E and Goncharov AF, Helium-hydrogen immiscibility at high pressures, J. Chem. Phys. 150,

114504 (2019).

8. Sukmas W, Pinsook U, Tsuppayakorn-ae P, Pakornchote T, Sukserm A, Bovornratanaraks T. Organic Molecule Orientations and Rashba-Dresselhaus Effect in alpha-Formamidinium Lead Iodide. *J. Phys. Chem. C* 123, 16508-15 (2019).

9. Jimlim P, Tsuppayakorn-ae P, Pakornchote T, Ektarawong A, Pinsook U and Bovornratanaraks T, Theoretical predictions for low-temperature phases, softening of phonons and elastic stiffnesses, and electronic properties of sodium peroxide under high pressure. *Rsc Adv.* 9, 30964-75 (2019).

10. Pakornchote T, Geballe ZM, Pinsook U, Taychatanapat T, Busayaporn W, Bovornratanaraks B and Goncharov AF, Raman spectroscopy on hydrogenated graphene under high pressure, *Carbon* 156, 549-57 (2019).

AWARD RECEIVED

2016 IUCr high-pressure workshop Young Scientist Award